A Measurement of the $\tau^- \to \mu^- \bar{\nu}_\mu \nu_\tau$ Branching Ratio

by

Laura Lee Kormos

B.Sc., University of Victoria, 1996.
M.Sc., University of Victoria, 1998.

A Dissertation Submitted in Partial Fulfillment of the
Requirements for the Degree of

DOCTOR OF PHILOSOPHY

in the Department of Physics and Astronomy.

We accept this thesis as conforming
to the required standard.

Dr. R. Sobie, Supervisor (Department of Physics and Astronomy)

Dr. R. Keeler, Co-Supervisor (Department of Physics and Astronomy)

Dr. R. Kowalewski, Departmental Member (Department of Physics and Astronomy)

Dr. D. Harrington, Outside Member (Department of Chemistry)

Dr. C. Hearty, External Examiner (University of British Columbia)

Supervisors: Dr. R. Sobie, Dr. R. Keeler

Abstract

The $\tau^- \to \mu^- \bar{\nu}_\mu \nu_\tau$ branching ratio has been measured using data collected from 1990 to 1995 by the OPAL detector at the LEP collider. The resulting value of

$$\mathrm{B}(\tau^- \to \mu^- \bar{\nu}_\mu \nu_\tau) = 0.1734 \pm 0.0009(stat) \pm 0.0006(syst)$$

has been used in conjunction with other OPAL measurements to test lepton universality, yielding the coupling constant ratios $g_\mu/g_\mathrm{e} = 1.0005 \pm 0.0044$ and $g_\tau/g_\mathrm{e} = 1.0031 \pm 0.0048$, in good agreement with the Standard Model prediction of unity. A value for the Michel parameter $\eta = 0.004 \pm 0.037$ has also been determined and used to find a limit for the mass of the charged Higgs boson, $m_{\mathrm{H}^\pm} > 1.28 \tan\beta$, in the Minimal Supersymmetric Standard Model.

Examiners:

Dr. R. Sobie, Supervisor (Department of Physics and Astronomy)

Dr. R. Keeler, Co-Supervisor (Department of Physics and Astronomy)

Dr. R. Kowalewski, Departmental Member (Department of Physics and Astronomy)

Dr. D. Harrington, Outside Member (Department of Chemistry)

Dr. C. Hearty, External Examiner (University of British Columbia)

Contents

List of Tables

List of Figures

Acknowledgements

I thank all of the members of the UVIC High Energy Physics group for making a lively, congenial working environment. I thank my supervisor, mentor, and valued friend, Randy Sobie, who has shown remarkable patience, understanding, and a persistent belief in my abilities over these many years. I thank my children who have matured and grown up to be lovely young adults in spite of coping with the extra stress of emotionally supporting me while I pursued a seemingly endless, self-flagellating journey toward a Ph.D. And I thank Ian Bailey, for his encouragement as my colleague, for his warmth, humour and strength as my most cherished friend, and for his love.

Chapter 1

Introduction

The universe around us provides an endlessly fascinating kaleidoscope of enigmas to titillate and tantalise the enquiring mind. Curiosity about this constantly shifting backdrop against which we play out our mundane lives can take various practical forms, from the study of stars and galaxies to the study of the fundamental particles[1] of nature. Particle physicists choose the latter option to satisfy their craving for understanding, by seeking to identify and measure the properties of the basic constituents of matter and to understand the natural laws which describe the forces that bind them to each other.

The Standard Model of Particle Physics has been formulated to describe the properties of elementary particles and the fundamental forces which govern the interactions between them. Within this model, the observed interactions of the fundamental particles are produced by the strong, weak, and electromagnetic forces. There is also a fourth fundamental force, gravity, which is insignificant at the mass or energy scales of experimental particle physics.

Fundamental particles within the Standard Model are of two basic types: those which make up the known matter in the universe, and those which act as "carriers"

[1]Fundamental particles are those with no observed substructure.

for the fundamental forces. The particles of which matter is formed are separated into two groups, leptons and quarks. Due to the nature of the strong interaction between them, quarks are not observed singly, but are observed in bound states of mesons or baryons, which have two or three quarks, respectively. An example of a meson is the pion, one of the components of cosmic ray showers, which is composed of a u and a d quark. The nucleons in an atom, protons and neutrons, are baryons and are composed of uud and udd quarks, respectively. Mesons and baryons are collectively known as hadrons. Leptons, which do not interact via the strong force, consist of electrons, e, muons, μ, tau particles, τ, and their associated neutrinos, ν_e, ν_μ, and ν_τ.

Of particular interest to this work is the τ lepton. The τ particle is by far the most massive lepton, and is observed to decay via approximately 50 measurable decay modes. Because of this relatively large decay phase space, the τ particle has a comparatively short lifetime of 290.6 fs [1]. It provides an experimentally clean environment in which to study and test many aspects of the Standard Model.

One such area of study involves the τ branching ratios. The fraction of τ particles that decay via a specific mode is the branching ratio for that mode. It is important to measure all of the τ branching ratios in order to have a complete picture of this particle and its interactions; but, in addition, an elegant test of the Standard Model can be constructed using the branching ratios of the decay of the τ to a muon and neutrinos, and to an electron and neutrinos. The analysis presented in this dissertation is a measurement of one such branching ratio, $\mathrm{B}(\tau^- \to \mu^- \bar{\nu}_\mu \nu_\tau)$, which is the fraction of τ particles that decays to a muon and two neutrinos.

Despite batteries of high-precision tests specifically designed to find a flaw in the Standard Model, it has remained unassailable, perhaps the only working model in existence which displays such an impressive range of verifiable predictive powers.

Every fundamental process and particle property that has been observed is consistent with the Standard Model.

However, there are theoretical indications that the Standard Model may be a low-energy approximation to an underlying theory. Among the problems of the Standard Model are its failure to predict the masses of the particles, and that the mechanism for producing massive particles involves a Higgs particle which has not yet been observed. The Standard Model and its limitations will be discussed more fully in Chapter 2.

Many of the fundamental particles are not readily available in nature, but rather must be produced by creating high-energy interactions between other particles. The τ particles used in this study were created using the Large Electron Positron (LEP) collider at the European Organisation for Nuclear Research (CERN) near Geneva, Switzerland. In the LEP collider, electrons and positrons were accelerated around a 27 km underground ring, and were brought into collision at four separate interaction points. Each of these interaction points housed a large particle detector, constructed to detect the particles produced in the electron-positron (e^+e^-) collision and to determine their identity based upon the ways in which they interact in the detector. One such detector is OPAL[2], which is described in detail in Chapter 3.

This work uses data taken by the OPAL detector from 1990 to 1995 at centre-of-mass energies near the mass of the Z^0 particle, resulting in the production of Z^0 particles at rest which subsequently decay in a variety of ways, one of which is to a $\tau^+\tau^-$ pair. In order to determine $B(\tau^- \to \mu^-\bar{\nu}_\mu\nu_\tau)$, a pure sample of $\tau^+\tau^-$ pairs is selected from the full LEP data set, and then the fraction of τ particles which have decayed to a muon and neutrinos is determined. This fraction is then corrected for backgrounds and efficiencies. The selection of $\tau^+\tau^-$ pairs is described in Chapter

[2]**O**mni-**P**urpose **A**pparatus for **LEP**

4, including a description of the modifications made in this work to the standard OPAL $\tau^+\tau^-$ selection; the selection of $\tau^- \to \mu^-\bar{\nu}_\mu\nu_\tau$ events is described in Chapter 5; and the determination of the branching ratio is described in Chapter 6. These latter sections detail the work done specifically for this analysis.

The measurement of $\mathrm{B}(\tau^- \to \mu^-\bar{\nu}_\mu\nu_\tau)$ presented in this work is the most precise measurement to date and has been published in reference [2]. When used in conjunction with other measurements, it provides a means of stringently testing the Standard Model. These tests are presented in Chapter 7.

Chapter 2

Theory

2.1 The Standard Model

The Standard Model of Particle Physics [3] is a quantum field theory in which the excitations of the fields describe the elementary particles. It is formulated as a Lagrangian equation which describes the interactions between the fundamental particles and predicts some of the particle properties. The beauty of the model lies in its elegance and its robustness. This robust nature can, however, be a two-edged sword.

The elegance of the Standard Model lies in the fact that the structure of each type of interaction between fundamental particles automatically arises out of the Standard Model Lagrangian when the requirement of local gauge invariance is imposed. This requirement demands that all of the observable physics be invariant under a transformation from one underlying state to another. The set of transformations that leave the physics unchanged is known as a group of symmetry operations or gauge transformations. For example, in electromagnetic theory it is possible to change the 4-vector field, A^{μ}, which is not observable, by adding to it the gradient of any arbitrary scalar function, without changing the measurable properties of the electric or magnetic fields. It is only our interpretation of what we observe that has changed.

The robustness of the Standard Model is evidenced by the fact that, despite a myriad of high-precision tests, no deviation from Standard Model predictions has ever been observed. The problem is that the Standard Model doesn't provide a complete description of nature, and experimental evidence of physics beyond the Standard Model would be a welcome indication as to which direction holds the complete theory for particle physics. Frustratingly, the very robustness of the Standard Model means that little directional information is forthcoming, although, with the current levels of precision being obtained in these tests, some areas of potentially new physics are constrained. The premise that one could perhaps begin anew, with a different model, and in that way test the very basics of the Standard Model, is a false one. There are so many ways in which the Standard Model agrees exactly with what we observe that any proposed model would have to either yield the same predictions but with fewer free parameters, or else yield predictions which do not contradict those of the Standard Model, and more.

Within the Standard Model, the constituents of matter are fermions (spin 1/2 particles). The particles which act as carriers for the fundamental forces arise out of the requirement of local gauge invariance and are gauge bosons (spin 1 particles). Each of the gauge bosons couples to a specific property termed "charge". The gauge boson of the electromagnetic force is the massless, chargeless photon, which couples to the familiar electric charge. Similarly, the gauge bosons for the strong force are massless gluons which couple to "colour charge". The gauge bosons of the weak force are the massive $W^{\pm}$ and Z^0 bosons which couple to "weak isospin charge".

	Leptons			Quarks		
Generation	Flavour	Charge	Mass(GeV)	Flavour	Charge	Mass
1	ν_e	0	$< 3 \times 10^{-9}$	u	$+\frac{2}{3}$	1.5 - 4.5 MeV
	e	-1	5.11×10^{-4}	d	$-\frac{1}{3}$	5 - 8.5 MeV
2	ν_μ	0	$< 1.9 \times 10^{-4}$	c	$+\frac{2}{3}$	1.0 - 1.4 GeV
	μ	-1	0.106	s	$-\frac{1}{3}$	80 - 155 MeV
3	ν_τ	0	$< 18 \times 10^{-3}$	t	$+\frac{2}{3}$	174.3 ± 5.1 GeV
	τ	-1	1.78	b	$-\frac{1}{3}$	4.0 - 4.5 GeV

Table 2.1: Some properties of the fundamental constituents of matter in the Standard Model. Electric charge is given in units of the positron (e^+) charge. The masses given are the Particle Data Book 2002 evaluations [1].

The fundamental fermions consist of six leptons and six quarks[1]. Each of these groups is divided into three *generations* in order of increasing mass[2]; each generation consists of a pair of leptons and a pair of quarks, the left-handed component of which forms an isospin doublet, as shown in Table 2.1. The leptons and quarks are differentiated from each other mainly by the way in which they interact. Quarks carry colour charge, weak isospin charge, and electric charge, and so may interact via the strong, weak, or electromagnetic forces. Leptons do not carry colour charge and so do not interact via the strong force, but do carry weak isospin charge and therefore interact via the weak force. In addition, charged leptons (those with electric charge) interact via the electromagnetic force. The bosons which mediate these forces are shown in Table 2.2.

[1]Each fundamental particle has an associated anti-particle with opposite electric charge. By a requirement known as *charge conjugation*, all other properties of a particle and its anti-particle partner are identical. In this work, wherever a process is shown for only one charged state, the opposite charged state is implied under charge conjugation.

[2]In this work, the units of $\hbar = c = 1$ are used; therefore, mass and momentum are in units of energy.

Force	Gauge boson
Electromagnetic	photons
Strong	gluons
Weak	$W^{\pm}/Z^0$

Table 2.2: Gauge bosons for the fundamental forces.

The Standard Model is based on a combination of three gauge groups, $SU_c(3) \times SU_L(2) \times U_Y(1)$. The form of the couplings between strongly interacting particles is described by $SU_c(3)$. The other two groups, $SU_L(2) \times U_Y(1)$, together describe the electroweak interaction. The subscript L indicates that only the left-handed chiral component of the fermions interacts with the W bosons. The subscript Y denotes the weak hypercharge of the particle, defined by $Q = T^3 + Y/2$, where Q is the electric charge and T^3 is the third component of the weak isospin. The left-handed components of the ν_e and e together form a left-handed weak isospin doublet, with $T^3_{\nu_e} = 1/2$ and $T^3_{\mathrm{e}} = -1/2$. The same is true for the u and d quarks, respectively, and the pattern holds throughout all three generations. The right-handed fermions are not part of the weak isospin doublets, but are singlets with $T = T^3 = 0$.

The Feynman diagrams for the interactions of the leptons and quarks via the fundamental forces are shown in Figure 2.1, where f stands for fermion, q stands for quark, l stands for lepton, q_{u} stands for any "up-type" ($T^3 = 1/2$) quark, and q_{d} stands for any "down-type" ($T^3 = -1/2$) quark. The probability of an interaction occuring is proportional to a characteristic coupling strength between the gauge boson and the fermions, given by g_{S}, g_{W}, g_{Z}, and g_{E} for the strong, charged-current weak, neutral-current weak, and electromagnetic interactions, respectively. The charged-current weak force proceeds via the exchange of a charged W boson and involves a

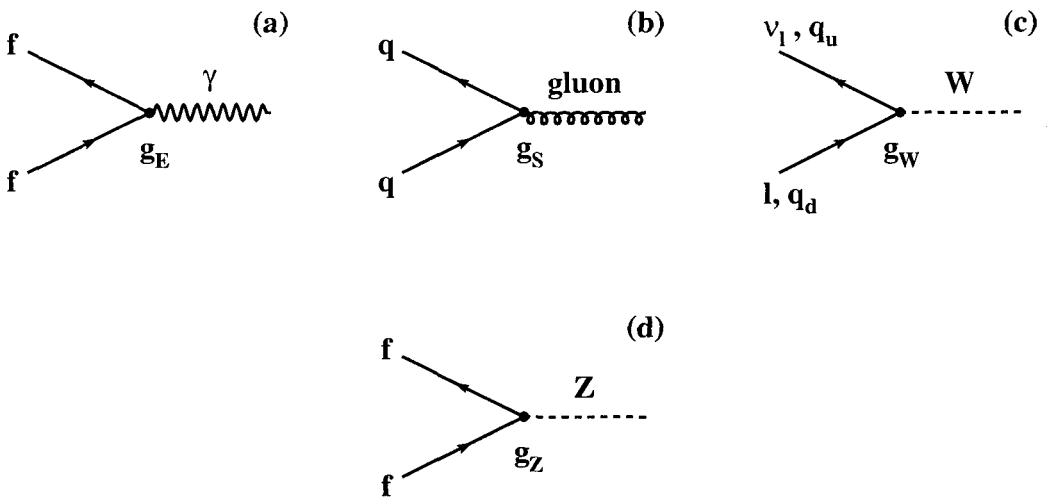

Figure 2.1: The Feynman diagrams for the (a) electromagnetic, (b) strong, (c) charged-current weak, and (d) neutral-current weak interactions.

rotation in the isospin doublet between the $T^3 = 1/2$ state and the $T^3 = -1/2$ state. Thus, these interactions may change the "flavour" of the particle from a neutrino to a charged lepton, or from an up-type quark to a down-type quark. Cross-generational changes are also permitted, with a probability determined by the elements in the 3×3 CKM matrix [4] for the quark sector. This is possible because the weak eigenstates are rotated with respect to the mass eigenstates which we observe. In the lepton sector, the neutrino mass is so small that until recently there was no indication that it was non-zero, and hence the properties of the cross-generational interactions are not yet known, but only are constrained by recent measurements to lie within certain parameter regimes [5].

Imposing the requirement of local gauge invariance on the Standard Model Lagrangian results in the prediction of massless gauge bosons for both the strong and

the electroweak forces. Although this agrees with experimental evidence in the case of the strong and electromagnetic forces, it does not agree in the case of the weak force, where the gauge bosons are massive. This theoretical problem was addressed by Glashow, Weinberg and Salam [3], and led to the introduction into the Standard Model of "spontaneous symmetry breaking". The mechanism of symmetry breaking requires that extra terms involving a new field be added to the Standard Model Lagrangian. This results in several changes to the Model: the electroweak force is separated into the electromagnetic force and the weak force as observed in nature; mass is imparted to the W and Z bosons; and the extra terms give rise to the prediction of a new massive boson which couples to mass, the Higgs particle, H^0 [6]. By introducing mass couplings into the Standard Model Lagrangian, this *Higgs mechanism* also generates the fermion masses.[3]

Unfortunately, the Higgs mechanism causes some problems within the Standard Model. For example, since the Higgs particle interacts with particles at the electroweak scale, it is natural to assume that its mass will be of the same order as that scale, or around 100 GeV. However, the radiative corrections to the Higgs mass, which are calculated by first order perturbation techniques, diverge quadratically (see, for example, [1, 7, 8]). In principle, this problem can be fixed within the Standard Model, but it requires some "fine tuning" at every order in perturbation theory, which lacks robustness. If it is important to include gravity in the theory, then the fine-tuning must extend to the Planck scale (10^{19} GeV), and the fine-tuning corrections become enormous.

The Standard Model is unsatisfactory in other ways as well. Table 2.1 shows a large mass hierarchy between generations, for which there is no theoretical basis. And

[3]No direct empirical evidence of any Higgs particle has yet been observed.

although the Standard Model predicts the forms of the couplings between particles, it does not predict their strength. It also does not predict the masses of the fermions. All of these properties must be entered into the Standard Model as free parameters, contributing to a total of 24 free parameters. Additionally, gravity is not included in the Standard Model of Particle Physics, but rather usually is described in terms of classical fields within a cosmological framework. These two areas overlap when considering the possible contributors to dark matter and to the cosmological constant, which is very poorly understood. Various theories are being tested which would refine the Standard Model and deepen our understanding of the universe at a fundamental level.

2.2 Beyond the Standard Model

In order to address some of the problems within the Standard Model, the mathematical concept of supersymmetry [9], in which each Standard Model particle has a partner whose spin differs by 1/2, was adopted. Since we do not observe a symmetry between bosons and fermions in nature, this symmetry must also be broken. The attractiveness of a supersymmetric theory is based in part upon the following: the extra particles contribute radiative corrections that cancel the problematic divergences in the Higgs mass mentioned above; demanding a local supersymmetry theory, which is analogous to imposing the requirement of local gauge invariance on the Standard Model Lagrangian, automatically brings gravity into the theory; and supersymmetry might provide a dark matter candidate, the lightest supersymmetric particle. In the Minimal Supersymmetric Standard Model, the existence of five Higgs bosons (h^0, H^0, $H^{\pm}$, A^0) is postulated, which is the minimal number required by a supersymmetry theory.

Another attractive aspect of supersymmetry is that it possibly provides a mechanism by which the forces may be unified, and so it is one of the Grand Unified Theory candidates. Unification of the forces implies that they can be described by a single coupling, or gauge group, and propagated by a single group of gauge bosons which couple to all of the fermions with one characteristic coupling strength. Clearly, this is not what we observe in the universe around us. Rather, we have (ignoring gravity) three forces mediated by three groups of gauge bosons. The strength of the coupling between the gauge bosons and the fermions for the strong, weak, and electromagnetic forces are given by the four different coupling constants g_S, g_W, g_Z, and g_E. It is hypothesized that, at high energies or temperatures such as those present in the early universe fractions of seconds after the big bang, these separate forces were unified, and then as the universe cooled and expanded the underlying symmetries were broken and the forces were resolved. There is some experimental support for this concept in the fact that the magnitudes of the coupling constants are dependent upon energy, and if supersymmetry theory is used to extrapolate their values to energies of the order of the Planck scale, they appear to converge.

2.3 The τ particle

Since its discovery in 1975 [10], the τ particle has provided a rich and interesting field of study for particle physicists. It is a third-generation sequential lepton; that is, its properties are identical to those of the first- and second-generation charged leptons, e and μ, with the exception of mass. Its relatively large mass allows it to decay to hadrons, as well as to the two lighter generations of leptons. The experimentally clean environment provided by the leptonic decays lends itself well to precise measurements of τ properties which can be used for stringent tests of the Standard Model. In figure

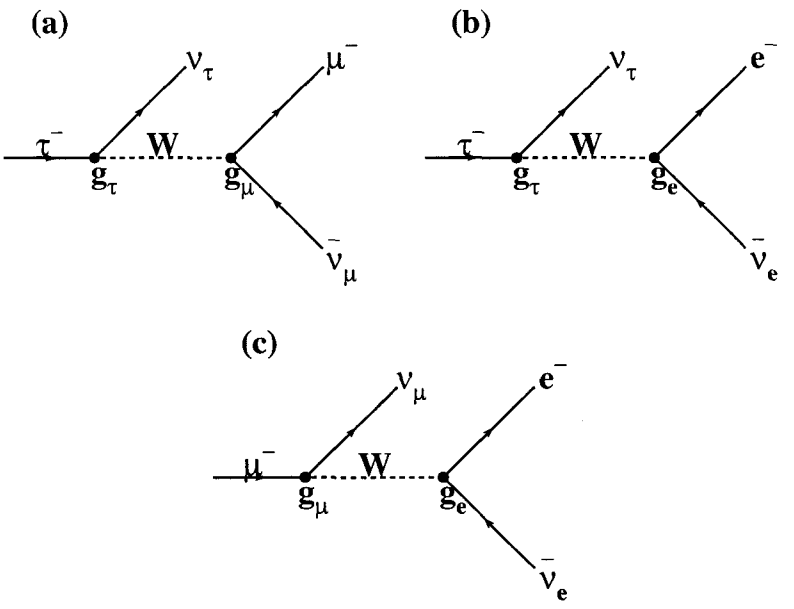

Figure 2.2: The Feynman diagrams for the decays (a) $\tau^- \to \mu^- \bar{\nu}_\mu \nu_\tau$, (b) $\tau^- \to e^- \bar{\nu}_e \nu_\tau$, and (c) $\mu^- \to e^- \bar{\nu}_e \nu_\mu$.

2.2, the Feynman diagrams are shown for the decays $\tau^- \to \mu^- \bar{\nu}_\mu \nu_\tau$, $\tau^- \to e^- \bar{\nu}_e \nu_\tau$, and $\mu^- \to e^- \bar{\nu}_e \nu_\mu$. In each case, the initial state particles are shown on the left and the final state particles are shown on the right.

The *partial decay width* of a particle is proportional to the transition rate from an initial state to a particular final state, and is obtained by integrating the differential width

$$d\Gamma = \frac{|\mathcal{M}|^2}{2m} d\phi \tag{2.1}$$

where $d\phi$ is the Lorentz invariant phase space factor which takes into account kinematic constraints such as conservation of 4-momentum, and m is the mass of the decaying particle. The matrix element, $\mathcal{M}$, takes into account the dynamics of the process such as the strength of the coupling between particles. For the decay

$\tau^- \rightarrow \mu^- \bar{\nu}_\mu \nu_\tau$ it is given by

$$\mathcal{M} = \left[\frac{-ig_\tau}{\sqrt{2}} \bar{\nu}_\tau \gamma_\mu \left(\frac{1-\gamma^5}{2}\right) \tau\right] \left(\frac{-i(g^{\mu\nu} - q^\mu q^\nu / M_W^2)}{q^2 - M_\mathrm{W}^2}\right) \left[\frac{-ig_\mu}{\sqrt{2}} \bar{\mu} \gamma_\nu \left(\frac{1-\gamma^5}{2}\right) \nu_\mu\right] \tag{2.2}$$

where $\bar{\nu}_\tau$, τ, $\bar{\mu}$, and ν_μ are Dirac spinors, γ_μ and γ^5 are Dirac matrices, q is the 4-momentum of the τ particle, and M_W is the mass of the W boson. The term in the first square brackets represents the coupling between the W and the (ν_τ, τ) doublet at the first vertex in Figure 2.2 (a), where the strength of the coupling is given by g_τ. The next term, in large parentheses, represents the W propagator. The term in the final square brackets represents the coupling between the W and the (ν_μ, μ) doublet at the final vertex in Figure 2.2 (a), where the strength of the coupling is given by g_μ. The term $q^\mu q^\nu$ arises from the polarisation modes of the W, and can be reduced to $m_\tau m_\mu$, the product of the masses of the charged leptons in the interaction. In the τ rest frame, $q^2 \approx m_\tau^2$. Since $m_\tau m_\mu << M_\mathrm{W}^2$ and $m_\tau^2 << M_\mathrm{W}^2$, Equation 2.2 reduces to

$$\mathcal{M} = \frac{-ig_\tau g_\mu}{8M_\mathrm{W}^2} \left[\bar{\nu}_\tau \gamma_\mu (1-\gamma^5)\tau\right] \left[\bar{\mu}\gamma^\mu (1-\gamma^5)\nu_\mu\right] \ . \tag{2.3}$$

Neglecting the masses of the final state leptons, averaging over the initial spin states, and summing over the final spin states, the $\tau^- \rightarrow \mu^- \bar{\nu}_\mu \nu_\tau$ partial width becomes

$$\Gamma(\tau^- \rightarrow \mu^- \bar{\nu}_\mu \nu_\tau) = \left(\frac{g_\tau g_\mu}{8M_\mathrm{W}^2}\right)^2 \frac{m_\tau^5}{96\pi^3} \ . \tag{2.4}$$

A more precise version of Equation 2.4 is obtained by including corrections for the muon mass, the full W propagator, and higher order processes [11], resulting in

$$\Gamma(\tau^- \rightarrow \mu^- \bar{\nu}_\mu \nu_\tau) = \left(\frac{g_\tau g_\mu}{8M_\mathrm{W}^2}\right)^2 \frac{m_\tau^5}{96\pi^3} \ f\left(\frac{m_\mu^2}{m_\tau^2}\right)(1 + \delta_\mathrm{RC}^\tau), \tag{2.5}$$

where the correction for the muon mass is

$$f(x) = 1 - 8x + 8x^3 - x^4 - 12x^2 \ln x. \tag{2.6}$$

The radiative correction term, $(1 + \delta^{\tau}_{\mathrm{RC}})$, in Equation 2.5 is given by

$$(1 + \delta^{\tau}_{\mathrm{RC}}) = \left[1 + \frac{\alpha(m_\tau)}{2\pi}\left(\frac{25}{4} - \pi^2\right)\right]\left[1 + \frac{3}{5}\frac{m_\tau^2}{m_{\mathrm{W}}^2}\right] \quad , \tag{2.7}$$

where $\alpha(m_\tau)$ is the electromagnetic coupling constant at the τ mass scale, and $(1 + \delta^{\tau}_{\mathrm{RC}}) = 0.99597$. The term in the first square brackets in Equation 2.7 takes into account photon radiative corrections, and the second term represents leading order W propagator corrections. The expressions for the decays $\tau^- \rightarrow \mathrm{e}^-\bar{\nu}_e\nu_\tau$ and $\mu^- \rightarrow \mathrm{e}^-\bar{\nu}_e\nu_\mu$ are analagous to those presented here.

Many particles can decay via more than one decay channel or mode. The branching ratio for a specific mode is given by the ratio of the partial decay width to the total decay width. For example, a τ particle decaying via the channel $\tau^- \rightarrow \mathrm{l}^-\bar{\nu}_l\nu_\tau$, where l stands for e or μ, has a corresponding branching ratio given by

$$B\left(\tau^- \rightarrow \mathrm{l}^-\bar{\nu}_l\nu_\tau\right) = \frac{\Gamma\left(\tau^- \rightarrow \mathrm{l}^-\bar{\nu}_l\nu_\tau\right)}{\Gamma_\tau}. \tag{2.8}$$

The total width Γ_τ in the denominator of Equation 2.8 is the inverse of the τ lifetime.

2.4 Testing the Standard Model

The Standard Model does not predict the magnitude of the couplings between the gauge bosons and the fermions. However, the couplings of the $W^{\pm}$ and Z^0 bosons to the different generations of leptons must be identical, or else gauge symmetry is lost and the model cannot predict the interactions or the forces. This prediction of *lepton universality* can be tested both in neutral-current weak processes which involve a Z^0 particle, and in charged-current weak processes which involve the $W^{\pm}$ particles. In this work, it will be tested in the latter process using leptonic τ decays. In addition, the leptonic τ branching ratios can be used to measure the Michel parameter η, which

can be used to set a limit on the mass of the charged Higgs particle in the Minimal Supersymmetric Standard Model. These topics are discussed below.

2.4.1 Lepton universality

The Standard Model prediction of lepton universality requires that the coupling constants shown at the vertices in Figure 2.2, g_{e}, g_{μ}, and g_{τ}, are identical and are all equal to g_W, thus the ratio g_{μ}/g_{e} is expected to be unity. This can be tested experimentally by taking the ratio of the corresponding branching ratios, which, by Equations 2.5 and 2.8, yields

$$\frac{\Gamma(\tau^- \to \mu^- \bar{\nu}_{\mu} \nu_{\tau})}{\Gamma(\tau^- \to \mathrm{e}^- \bar{\nu}_{e} \nu_{\tau})} = \frac{\mathrm{B}(\tau^- \to \mu^- \bar{\nu}_{\mu} \nu_{\tau})}{\mathrm{B}(\tau^- \to \mathrm{e}^- \bar{\nu}_{e} \nu_{\tau})} = \frac{g_{\mu}^2}{g_{\mathrm{e}}^2} \left[\frac{f\left(\frac{m_{\mu}^2}{m_{\tau}^2}\right)}{f\left(\frac{m_{\mathrm{e}}^2}{m_{\tau}^2}\right)} \right] . \tag{2.9}$$

In addition, the expressions for the partial widths of the $\tau^- \to \mu^- \bar{\nu}_{\mu} \nu_{\tau}$ and $\mu^- \to \mathrm{e}^- \bar{\nu}_{e} \nu_{\mu}$ decays can be rearranged to test lepton universality between the first and third lepton generations, yielding the expression

$$\frac{g_{\tau}^2}{g_{\mathrm{e}}^2} = \mathrm{B}(\tau^- \to \mu^- \bar{\nu}_{\mu} \nu_{\tau}) \frac{m_{\mu}^5}{m_{\tau}^5} \frac{\tau_{\mu}}{\tau_{\tau}} \frac{f\left(\frac{m_{\mathrm{e}}^2}{m_{\mu}^2}\right)}{f\left(\frac{m_{\mu}^2}{m_{\tau}^2}\right)} \frac{(1+\delta_{\mathrm{RC}}^{\mu})}{(1+\delta_{\mathrm{RC}}^{\tau})} . \tag{2.10}$$

2.4.2 Michel parameter η and the charged Higgs mass

The most general form of the matrix element for τ leptonic decay involves all possible combinations of scalar, vector, and tensor couplings to left- and right-handed particles (see, for example, [12]), and is given by

$$\mathcal{M} = \frac{4 G_{\mathrm{F}}}{\sqrt{2}} \sum_{\gamma=\mathrm{S,V,T}} \sum_{i,j=\mathrm{L,R}} g_{i,j}^{\gamma} (\bar{l} \Gamma^{\gamma} \nu_l)(\bar{\nu}_{\tau} \Gamma_{\gamma} \tau_j) \tag{2.11}$$

where

$$\Gamma^{\mathrm{S}} = 1, \quad \Gamma^{\mathrm{V}} = \gamma^{\mu}, \quad \Gamma^{\mathrm{T}} = \tfrac{i}{2\sqrt{2}} [\gamma^{\mu} \gamma^{\nu} - \gamma^{\nu} \gamma^{\mu}],$$

and $G_{\rm F}$ is the Fermi coupling constant. In the Standard Model, the coupling terms take the following values: $g^{\rm V}_{\rm LL} = 1$ and all other $g^{\gamma}_{i,j} = 0$, where γ = S, V, or T for scalar, vector, or tensor couplings, and i, j = L or R for the chirality of the initial and final state charged leptons. These coupling terms represent the relative contribution of each particular type of coupling to the overall coupling strength, $G_{\rm F}$.

The shape of the τ leptonic decay spectrum can be parameterized in terms of the four Michel parameters [13, 14], η, ρ, ξ, and δ. The partial decay width of $\tau^- \to l^- \bar{\nu}_l \nu_\tau$ in the laboratory reference frame can be expressed in terms of the Michel parameters as [1]

$$\frac{d\Gamma_l}{dx} = \frac{G_{\rm F}^2 m_\tau^5}{192\pi^3} \times \left\{ f_0(x) + \rho f_1(x) + \eta \frac{m_l}{m_\tau} f_2(x) - P_\tau [\xi g_1(x) + \xi\delta g_2(x)] \right\} \qquad (2.12)$$

where l is e or μ, $x \equiv E_l / E_{l,\rm max}$, and f_i and g_i are polynomials defined in reference [1]. E_l is the energy of the charged daughter lepton and $E_{l,\rm max}$ is taken to be the beam energy. The integrated decay width in terms of the Standard Model decay width, $\Gamma_l^{(\rm SM)}$, is given by

$$\Gamma_l = \frac{G_{\rm F}^2 m_\tau^5}{192\pi^3} \left(1 + 4\eta \frac{m_l}{m_\tau} \right) = \Gamma_l^{(\rm SM)} (1 + 4\eta \frac{m_l}{m_\tau}). \qquad (2.13)$$

The Michel parameter η is given by

$$\eta = \frac{1}{2} Re \left\{ g^{\rm V}_{\rm LL}\, g^{\rm S*}_{\rm RR} + g^{\rm V}_{\rm RR}\, g^{\rm S*}_{\rm LL} + g^{\rm V}_{\rm RL} (g^{\rm S*}_{\rm LR} + 6 g^{\rm T*}_{\rm LR}) + g^{\rm V}_{\rm LR} (g^{\rm S*}_{\rm RL} + 6 g^{\rm T*}_{\rm RL}) \right\}, \qquad (2.14)$$

and hence its Standard Model value is zero. A non-zero value of η would affect the τ decay width via its contribution to Equation 2.13. The term involving the ratio of masses in Equation 2.13 acts as an effective suppression factor in the case of $\tau^- \to {\rm e}^- \bar{\nu}_e \nu_\tau$ decays; however, the same is not true in $\tau^- \to \mu^- \bar{\nu}_\mu \nu_\tau$ decays. It is possible then to solve for η by taking the ratio $\Gamma_\mu(\eta)/\Gamma_{\rm e}(\eta)$, or equivalently by taking

the ratio of the measured branching ratios [15]. Using Equations 2.5 and 2.13, we find

$$\frac{\mathrm{B}(\tau^- \to \mu^- \bar{\nu}_\mu \nu_\tau)}{\mathrm{B}(\tau^- \to \mathrm{e}^- \bar{\nu}_e \nu_\tau)} = 0.9726 \left(1 + 4\eta \frac{m_\mu}{m_\tau}\right) \tag{2.15}$$

where m_e/m_τ is taken to be zero and assuming lepton universality ($g_\mu = g_\mathrm{e}$).

In addition, if one assumes that the first term in the expression for η is non-zero, then there must be a non-zero scalar coupling constant, such that $\eta = \frac{1}{2} Re\{g^{\mathrm{S}*}_{\mathrm{RR}}\}$. This coupling constant has been related to the mass of a charged Higgs particle in the Minimal Supersymmetric Standard Model via the expression

$$g^{\mathrm{S}}_{\mathrm{RR}} = -m_l m_\tau (\tan\beta / m_{\mathrm{H}^\pm})^2, \tag{2.16}$$

where $\tan\beta$ is the ratio of the vacuum expectation values of the two Higgs fields. η can be approximately written as [15]

$$\eta = -\frac{m_\tau m_\mu}{2} \left(\frac{\tan\beta}{m^{\pm}_{\mathrm{H}}}\right)^2. \tag{2.17}$$

Thus, η can be used to place constraints on the mass of the charged Higgs.

Chapter 3

The OPAL experiment

The data used in this work were produced at the CERN experimental facility, on the France-Switzerland border near Geneva, Switzerland. Founded in 1954, this facility is maintained through international collaboration and is dedicated to the pursuit of both fundamental particle physics knowledge, and the export of this knowledge along with the associated technological skills to industrial fields. CERN provides the accelerators necessary to create exotic particles such as τ leptons. This chapter describes the LEP collider and the OPAL detector which was used to identify and to determine the properties of the τ particles through the measurement of their decay products.

3.1 The LEP collider

The LEP collider was a facility consisting of several particle accelerators which worked in stages to produce and store electrons and positrons, and collide them at high energies. From 1989 to 1995, LEP operated at a centre-of-mass energy of approximately 90 GeV (LEP1). From 1995 to 2000, the centre-of-mass energy was increased in steps up to approximately 209 GeV (LEP2). In this work, only LEP1 data was used.

The collider had two main sections: the injector chain, which produced, stored,

and accelerated electrons and positrons to 20 GeV, and the main (LEP) ring which accelerated them to approximately 45 GeV, thereby providing the centre-of-mass energy of approximately 90 GeV needed for Z^0 production.

Figure 3.1 shows the injector chain and the LEP ring. Positrons were produced by bombarding the converter target with 200 MeV electrons from a linear accelerator (linac). The electrons and positrons were then accelerated in another linac (LIL) to 600 MeV, after which they were collected in the Electron Positron Accumulator (EPA). They were subsequently injected in bunches, or pulsed, into the Proton Synchrotron (PS) where their energy was increased to 3.5 GeV, and then were transferred to the Super Proton Synchrotron (SPS) where they were accelerated to 20 GeV. The final stage of the process occurred in the LEP ring, where they were accelerated to 45 GeV.

The LEP collider was operated in eight-bunch mode, in which the electron and positron beams were injected into the LEP ring as eight equally-spaced bunches. Prior to 1992, four bunch mode was used. Each bunch had approximately 4×10^{11} particles and completed a revolution in 89μs. The beams were made to collide in four interaction areas, one of which housed the OPAL detector. The positions of OPAL and the other detectors, ALEPH[1], L3[2], and DELPHI[3] are shown on Figure 3.1.

---

[1] **A**pparatus for **LEP** **Ph**ysics

[2] **LEP 3** experiment

[3] **D**etector with **L**epton **P**hoton and **H**adron **I**dentification

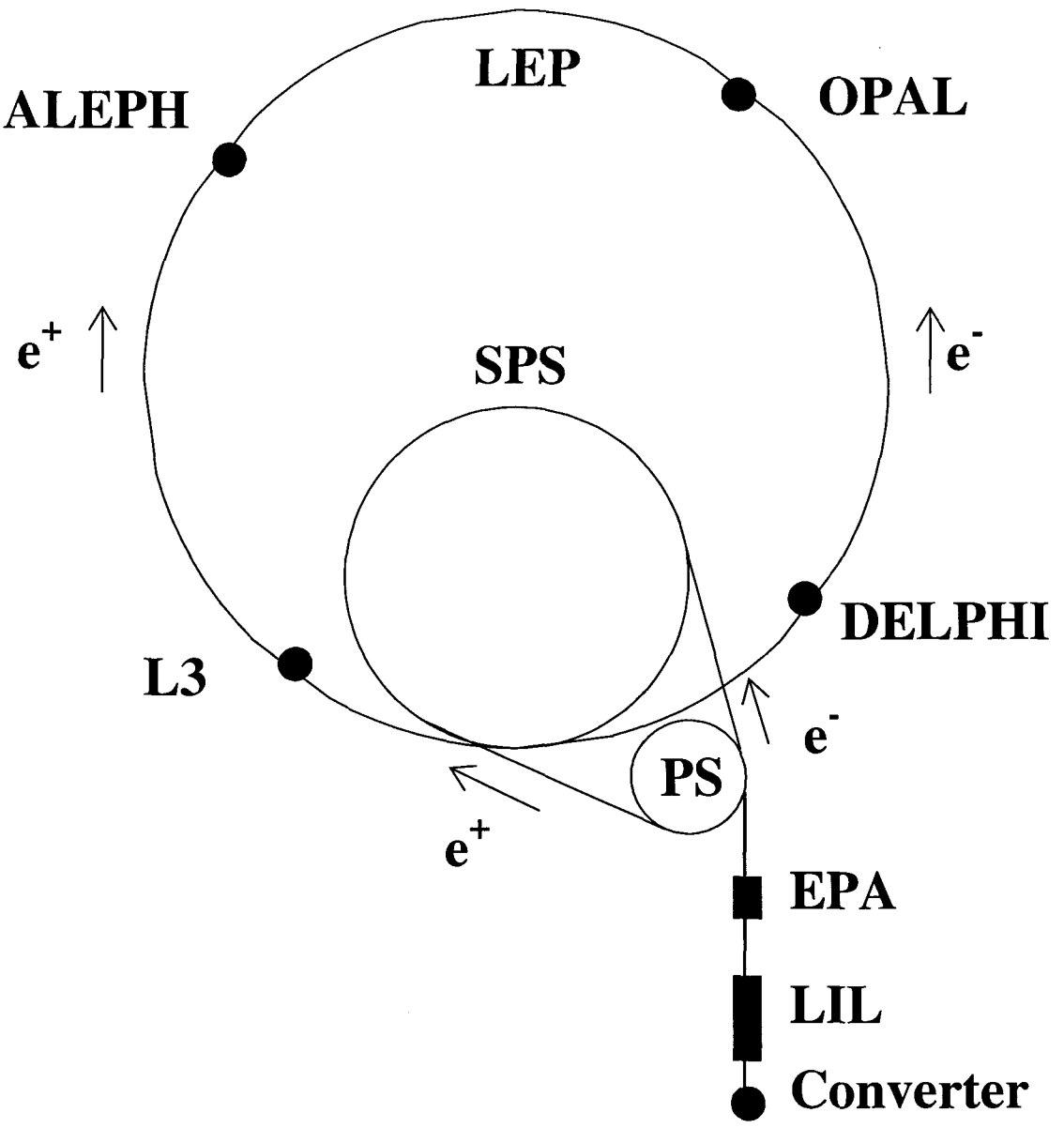

Figure 3.1: Schematic view of the injection scheme and the LEP ring, along with the locations of the four experimental areas.

3.2 The OPAL detector

OPAL [16] is a general purpose detector covering almost the full solid angle with approximate cylindrical symmetry about the e^+e^- beam axis[4]. Figure 3.2 is a schematic diagram of OPAL. The following subdetectors are of particular interest in this analysis: the tracking system, the electromagnetic calorimeter, the hadronic calorimeter, and the muon chambers. The tracking system includes two vertex detectors, z-chambers, and a large volume cylindrical tracking drift chamber surrounded by a solenoidal magnet which provides a magnetic field of 0.435 T. This system is used to determine the particle momentum and rate of energy loss, and provides information which makes it possible to reconstruct the trajectories (tracks) of charged particles traversing the detector. The electromagnetic calorimeter consists of lead-glass blocks backed by photomultiplier tubes or photo-triodes for the detection of Čerenkov radiation emitted by relativistic particles. The instrumented magnet return yoke serves as a hadronic calorimeter, consisting of up to nine layers of limited streamer tubes sandwiching eight layers of iron, with inductive readout of the tubes onto large pads and aluminium strips. In the central region of the detector, the calorimeters are surrounded by four layers of drift chambers for the detection of muons emerging from the hadronic calorimeter. In each of the forward regions, the muon detector consists of four layers of limited streamer tubes arranged into quadrants which are transverse to the beam direction. A more detailed description of each of these subdetectors follows, beginning at the vacuum beam pipe and proceeding radially outward.

[4]In the OPAL coordinate system, the e^- beam direction defines the $+z$ axis, and the $+x$ axis points from the detector toward the centre of the LEP ring. The polar angle θ is measured from the $+z$ axis and the azimuthal angle ϕ is measured from the $+x$ axis. The origin of the coordinate system is located at the nominal interaction point in the centre of the detector.

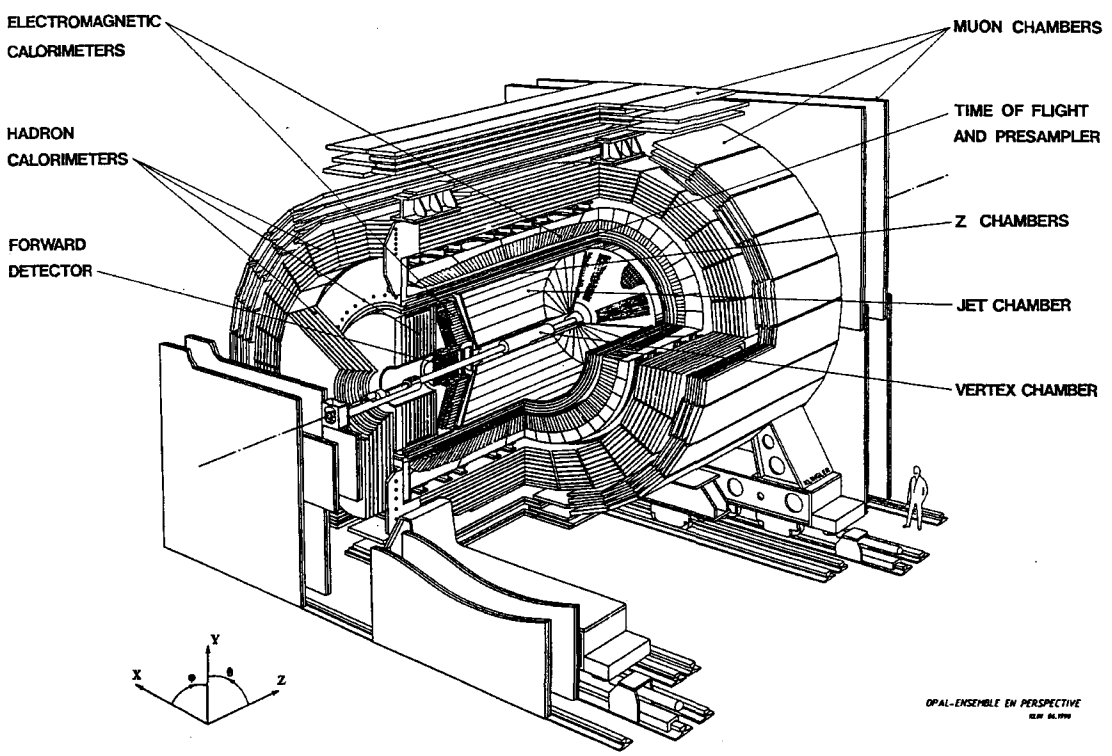

Figure 3.2: A cut away view of the OPAL detector showing its main components. The electron beam runs along the $+z$ axis and the $+x$ axis points to the centre of the LEP ring. The e^+e^- interaction point is in the centre of the detector.

3.2.1 The central tracking system

The central tracking system includes a silicon microvertex detector which is co-axial to an evacuated pipe with radius 5.35 cm through which the beam travels, followed by a pressure vessel holding the central vertex detector, jet chamber, and z-chambers. The gas in the pressure vessel is held at four bars.

The silicon microvertex detector

The innermost detector is the silicon microvertex detector, which consists of two barrels of double-sided silicon microstrip detectors at radii of 6 and 7.5 cm [16, 17]. The inner layer consists of 11 "ladders" arranged azimuthally around the beam pipe, and the outer layer consists of 14 ladders. The ladders overlap to avoid gaps in the ϕ coverage. Each ladder consists of three silicon wafers daisy-chained together. Each wafer is a pair of single-sided silicon detectors 33 mm wide and 60 mm long glued back-to-back. One side has readout strips running longitudinally (in the z direction) in order to measure the ϕ position, while the other side has readout strips running azimuthally in order to measure the z position.

A charged particle entering the silicon detector deposits charge, which is measured by electronic equipment at the end of each ladder. The silicon detector has a track position resolution of 10 μm in ϕ and 15 μm in z, and helps to pinpoint the location of the primary vertex, the point at which the e^+e^- collision occurred.

The central vertex detector

The 1 m long central vertex detector is the first of the detectors within the pressure vessel and extends from the inner wall of the pressure vessel (at a radius of 8.8 cm) to a radius of 23.5 cm. It consists of an inner axial region and an outer stereo region,

each divided into 36 sectors in ϕ. The sectors of the inner region each contain a plane of 12 sense wires strung parallel to the beam and ranging radially outward from 10.3 to 16.2 cm. The stereo sectors lie between radii of 18.8 and 21.3 cm, each containing a plane of 6 sense wires each of which is inclined at an angle of approximately 4° relative to the z-direction. A charged particle moving through the detector ionizes the ambient gas. The resulting ions drift to the charged wires; a precise measurement of the drift time to the axial wires allows the $r - \phi$ position to be calculated to within 50μm [16]. The time difference of the signal's arrival at opposite ends of an axial wire provides an estimate of the z position which is used by the OPAL track trigger and in pattern recognition. An accurate z measurement is found by combining the information from the axial and the stereo sectors, which provides a resolution of 700μm.

The tracking chamber

The central jet chamber, or tracking chamber, is a large volume cylindrical drift chamber 4 m long, with an inner radius of 25 cm and an outer radius of 185 cm. The chamber is divided into 24 sectors in ϕ. Each sector contains a sense wire plane extending radially outward with 159 anode wires strung parallel to the beam direction, and two cathode planes which form the boundaries between adjacent sectors [16]. The ionization of the gas caused by the passage of a charged particle results in charges being collected on the anode wires. The integrated charge collected is measured at each end of the wire; the ratio of these two measurements for a given wire determines the z position of the particle's track. The $r-\phi$ position is determined by the position of the wire and the drift time to the wire, respectively. This provides a resolution of 135 μm in $r - \phi$ and 6 cm in z [16].

The chamber is in a known magnetic field and hence the track curvature can be used to find the momentum of the particle. The resolution of momentum measurements was found to be

$$\frac{\sigma_p}{p^2} = 2.2 \times 10^{-3} \mathrm{GeV}^{-1} \tag{3.1}$$

where momentum p is in GeV.

A particle loses energy as it ionizes the gas. The rate of energy loss, $\mathrm{d}E/\mathrm{d}x$, is a function of particle type (electrons, muons, pions, kaons, and protons) and is momentum dependent. It is measured using the total charge collected on the anode wires. The four bar pressure of the gas was chosen to optimize the tracking resolution and the $\mathrm{d}E/\mathrm{d}x$ measurement, that is, to increase the probability of the particle interacting while limiting the effects of multiple scattering. Figure 3.3 shows the dependence of $\mathrm{d}E/\mathrm{d}x$ on momentum for the particle species listed above. The measured points are in good agreement with the theoretical expectation.

The z-chambers

The last of the subdetectors within the pressure vessel, the z-chambers provide a precise measurement of the z position of particle tracks. They consist of 24 drift chambers, each 4 m long and divided in the z direction into eight cells. Each cell has six anode wires running in the ϕ direction and placed at increasing radii. Measurements of the drift time to the wire, and the wire position give a z measurement with a resolution of 300 μm.

The overall tracking resolution

The tracking system without the silicon detector provides a resolution of 75 μm in the $r - \phi$ plane and 2 mm in the $r - z$ plane [16]. With the silicon detector, the

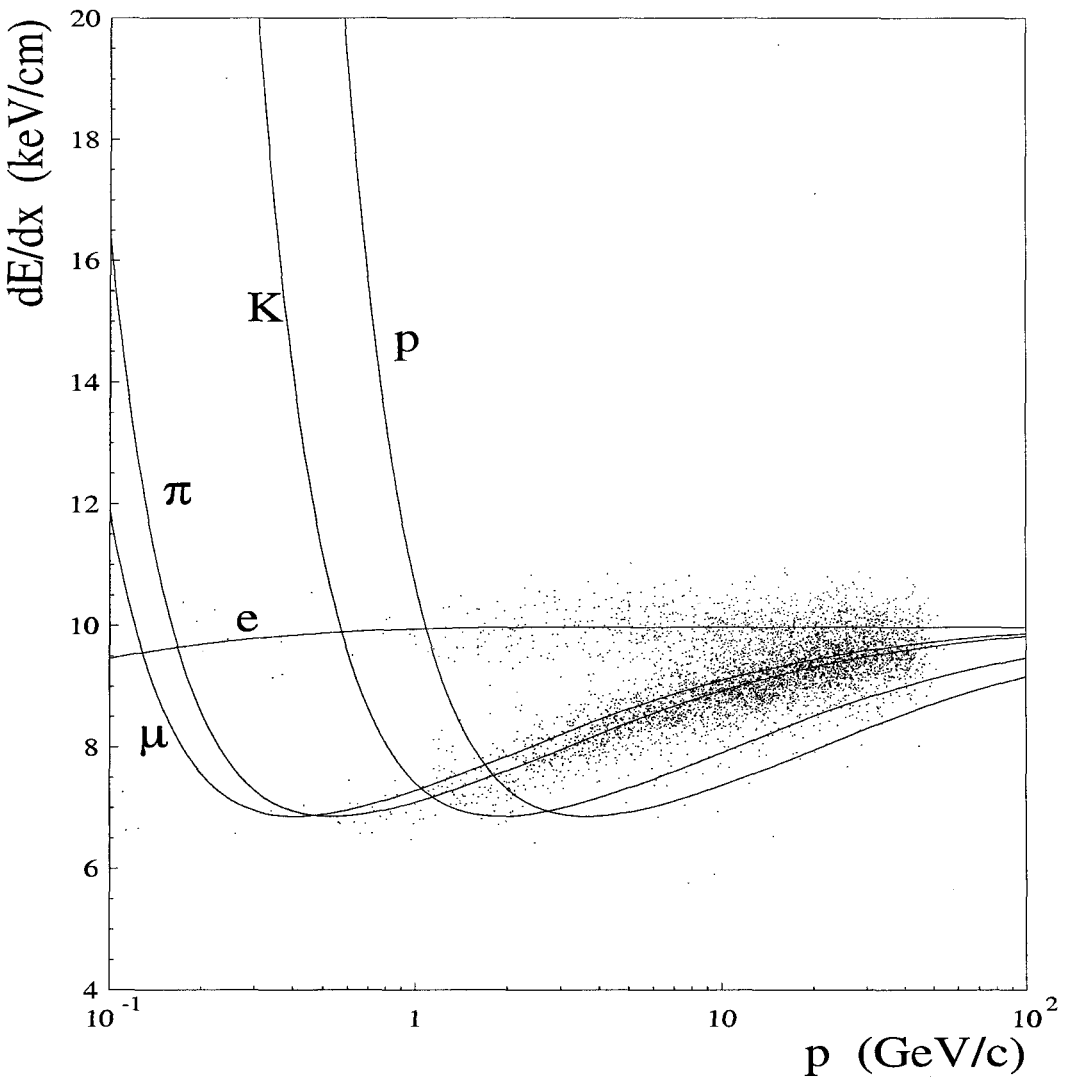

Figure 3.3: Ionization measurements ($\mathrm{d}E/\mathrm{d}x$) for various particle species. Theory curves are overlaid with real data (points).

resolution of the impact parameter measurement is 15 μm in the $r - \phi$ plane, and resolution in the z direction is $20 - 50$ μm[17].

3.2.2 The solenoidal magnet and time-of-flight detector

Immediately outside the pressure vessel lies the magnet, which consists of a solenoidal coil and an iron yoke. The coil provides a uniform magnetic field of 0.435 T aligned with the electron beam. The magnetic flux is returned through the iron yoke.

The time-of-flight system forms a barrel around the outside of the solenoid, consisting of 160 scintillation counters each 6.840 m long at a mean radius of 2.360 m. Each counter has a trapezoidal cross-section, 45 mm thick $\times$ 89 to 91 mm wide. These are used to measure the time of flight of a particle from the interaction region, which allows for the rejection of cosmic ray events. The time-of-flight system is used in the OPAL trigger; a time-of-flight signal within 50 ns of a known beam crossing time is required for a good event.

3.2.3 The electromagnetic calorimeter

The lead glass electromagnetic calorimeter measures the energies and positions of electrons, positrons and photons. A photon or electron is expected on average to lose all of its energy in the electromagnetic calorimeter.

Before entering the lead glass calorimeter, particles pass through approximately two radiation lengths[5] of material, due mostly to the solenoidal coil and the wall of the pressure vessel. Thus, most electromagnetic showers begin before the lead glass itself. To compensate for this, presamplers are installed immediately in front of the lead glass to measure the position and energy of these electromagnetic showers. The

[5]A radiation length is the distance in which an electron's energy is reduced by a factor of e by bremsstrahlung radiation as it passes through a material.

presampler is composed of wire chambers, and is able to improve the electromagnetic energy resolution of a shower because the pulse height observed by the device is proportional to the number of charged particles traversing it.

The barrel region of the lead glass electromagnetic calorimeter covers the region $|\cos\theta| < 0.82$ and consists of a cylindrical array of lead glass blocks each of length 37 cm (equal to 24.6 radiation lengths), positioned at a radius of 2.455 m [16]. The longitudinal axes of the blocks point toward the interaction region. The cross-sectional area of each of the blocks transverse to the longitudinal direction is 10 cm $\times$ 10 cm. Each lead glass block is backed by a light guide, and then a phototube which detects the Čerenkov radiation produced in the glass by relativistic particles. The endcap electromagnetic calorimeter consists of two dome-shaped arrays of lead glass blocks. It differs from the barrel lead glass calorimeter in that the axes of the blocks are coaxial with the beam line, as opposed to the quasi-pointing geometry of the barrel region, and the blocks are backed by vacuum photo triodes rather than light guides and phototubes. The blocks range in length from 380 mm to 520 mm and are arranged over the endcap to give a total depth of at least 20.5 radiation lengths of coverage. The energy resolution of the lead glass calorimeter without any material in front was found to be $\sigma_E/E = 0.002 + 0.063 GeV^{\frac{1}{2}}/\sqrt{E}$, where E is measured in GeV [16]. However, the two radiation lengths of material in front of it substantially degrades the energy resolution of the electromagnetic calorimeter.

3.2.4 The hadronic calorimeter

Surrounding the electromagnetic calorimeter is the iron return yoke of the magnet, which is interleaved with detector chambers to form a cylindrical sampling hadronic calorimeter from radii 3.39 m to 4.39 m. The barrel region of this calorimeter lies

within the region $|\cos\theta| < 0.81$, and consists of nine layers of limited streamer tubes sandwiching eight layers of iron, segmented into 24 wedge-shaped sectors in ϕ. Layers two through eight consist of half-length chambers, each about 5 m long, with a junction near the equator of the detector at approximately $\theta = 90^{\circ}$. The junctions of alternate layers are staggered to provide more complete coverage. Layers one and nine are constructed from single chambers, each about 7.3 m long and centred at $\theta = 90^{\circ}$. The barrel region is closed at each end by a doughnut-shaped endcap which covers the region $0.81 < |\cos\theta| < 0.91$ and consists of eight layers of streamer tubes sandwiching seven layers of iron. The return yoke in the hadronic calorimeter provides four or more interaction lengths[6] of absorber. Because of the 2.2 interaction lengths of material before the hadronic calorimeter, the energy of a hadron will include a component in the electromagnetic as well as the hadronic calorimeter. Almost all hadrons will be absorbed at this stage, leaving mainly muons to pass on to the muon chambers [16].

3.2.5 The muon chambers

The barrel region of the hadronic calorimeter is surrounded by 110 large drift chambers, each 1.2 m wide, 90 mm thick, and between 6.0 and 10.4 m long, arranged in four layers for the purpose of detecting muons. These muon chambers cover the region $|\cos\theta| < 0.68$ for all four layers, or $|\cos\theta| < 0.72$ for at least one layer. Each chamber consists of two side-by-side longitudinal cells, each with an anode wire that runs the full length of the chamber. Above and below the anode wire are diamond-shaped cathode pads which are used to determine the longitudinal coordinate, z, to a precision of 2 mm. The ϕ coordinate is determined by the drift time, to a precision

[6] An interaction length is the mean free path of a particle before undergoing a nuclear collision.

of 1.5 mm.

The endcap muon detectors cover the region $0.67 < |\cos\theta| < 0.98$, each endcap consisting of two layers of 6 m $\times$ 6 m quadrant chambers and two layers of 3 m $\times$ 2.5 m patch chambers. Each quadrant chamber and patch chamber has two layers of limited streamer tubes, so that each endcap has at least four layers of active detector. Within each quadrant layer, the quadrants overlap vertically to provide more complete coverage, but cannot overlap horizontally due to the presence of the beam pipe, shielding, cables, and support structures. This is partly remedied by the patch chambers, which cover much of the gap between the quadrant chambers; however, regions without particle detection capabilities do remain, as discussed in Appendix A. Within each chamber, the two layers of streamer tubes are perpendicular to the beam axis, one layer having horizontal wires and the other having vertical wires.

Chapter 4

The $\tau^+\tau^-$ selection

At LEP1, electrons and positrons were made to collide at centre-of-mass energies close to the Z^0 peak, producing Z^0 bosons at rest which subsequently decayed into back-to-back pairs of charged leptons (e^+e^-, $\mu^+\mu^-$, $\tau^+\tau^-$), neutrinos ($\nu_e\bar{\nu}_e$, $\nu_\mu\bar{\nu}_\mu$, $\nu_\tau\bar{\nu}_\tau$), or quarks ($q\bar{q}$) which produce multihadron events. The branching ratio for each of these modes of decay is about 10.1 percent for the combined charged lepton channels, 20 percent for the combined neutrino channels, and 69.9 percent for the combined quark channels [1]. The highly relativistic τ particles decay in flight close to the interaction point, resulting in two highly-collimated, back-to-back streams of particles, or jets, in the detector.

For this analysis, the $e^+e^- \rightarrow \tau^+\tau^-$ events are selected from the full LEP1 data set, and then the fraction of τ jets in which the τ has decayed to a muon is determined. This fraction is then corrected for backgrounds in both the $\tau^+\tau^-$ sample and in the $\tau^- \rightarrow \mu^-\bar{\nu}_\mu\nu_\tau$ sample, and efficiencies. These corrections involve the use of Monte Carlo simulated events. The Monte Carlo simulated events are processed using the same selections as the LEP1 data, in order to maintain uniformity with the data. This chapter describes the LEP1 data, the simulated events, the $\tau^+\tau^-$ selection, the background remaining in the $\tau^+\tau^-$ sample, and the corresponding error estimate.

4.1 The LEP1 data

The OPAL trigger identified events of interest which were then recorded for further processing, corresponding to an integrated luminosity[1] of approximately 173 pb^{-1}. Most subdetectors and other associated trigger hardware were required to be in good running order at the time of data-taking for the measurements to be used in the $\tau^+\tau^-$ selection. To this end, there are four status levels defined for each: 0 indicates that the status is unknown, 1 indicates that the unit is off, 2 indicates that the unit is partially operating (some subdetectors may have had regions that no longer were operative), and 3 means the subdetector or trigger was fully functioning. The minimum levels required for each subdetector and trigger used in the $\tau^+\tau^-$ selection are shown in Table 4.1. If no requirement was placed on a particular trigger, the trigger status is left blank. The top line names the pertinent subdetector; the abbreviations are for the central vertex detector (CV), central jet tracking chamber (CJ), time-of-flight system (TB), presampler (PB), barrel electromagnetic calorimeter (EB), endcap electromagnetic calorimeter (EE), hadronic calorimeter strips (HS), barrel muon chambers (MB), and endcap muon chambers (ME). As indicated in the table, OPAL data was taken if CJ, EB, and EE were close to fully operational.

	CV	CJ	TB	PB	EB	EE	HS	MB	ME
Detector Status	3	3	3	2	3	3	3	3	3
Trigger Status		2			2	3			

Table 4.1: Detector and trigger status levels required in the $\tau^+\tau^-$ selection.

[1]Luminosity is the flux of particles in units of number of particles per barn per second, where 1 barn = 10^{-28} m^2. The integrated luminosity is the total luminosity recorded by OPAL during the entire LEP1 running period. The number of events of a particular type is given by $N = \sigma L$, where σ is the cross-section for that particular reaction (in barns) and is related to the probability of the reaction occuring, and L is the luminosity.

4.2 The Monte Carlo simulated events

Monte Carlo simulations are used to model both the signal and background events. Comparing the data with these models allows for the measurement of efficiencies and backgrounds. A total of 2,275,000 Monte Carlo $e^+e^- \to \tau^+\tau^-$ events were generated using KORALZ, a Monte Carlo program which creates four-vector quantities [18]. Once the four-vector momenta of the τ's have been generated, the TAUOLA [19] program is called to simulate the decay of the τ's using the τ branching ratios. Background contributions from non-τ sources were evaluated using Monte Carlo samples based on the following generators: multihadron events ($e^+e^- \to q\bar{q}$) were simulated using JETSET 7.3 and JETSET 7.4 [20], dimuon events using KORALZ [18], Bhabha events using BHWIDE [21], and two-photon events using VERMASEREN [22]. These background events are discussed more fully in the next section.

The four-vectors produced by these generators are then processed by the OPAL detector simulation program GOPAL, which uses the CERN library package GEANT to simulate the detector's response to the Monte Carlo particles [23]. After this stage of processing, the simulated detector responses are in exactly the same format as the OPAL data collected from LEP, and the simulated events are henceforth processed using the same reconstruction program (ROPE) as the data.

4.3 The $\tau^+\tau^-$ selection

This analysis uses the standard OPAL $\tau^+\tau^-$ selection [24], with slight modifications for the rejection of Bhabha events, as described in Section 4.3.2. The selection places specific constraints on the properties of tracks and of electromagnetic clusters, which are localised regions of activity in the electromagnetic calorimeter. In order to be

considered a "good" track or a "good" cluster, the criteria listed in Table 4.2 must be satisfied. The tracking requirement helps to remove cosmic ray events from the sample by requiring that the tracks point to the origin.

Selection	Requirement	Description
Good track definition	$N_{CJ}^{hits} \geq 20$	Number of hits in the central jet chamber.
	$P_T \geq 0.1$ GeV	Momentum transverse to the beam direction.
	$\|d_0\| \leq 2$ cm	Distance to the beam axis at the point of closest approach in the $r-\phi$ plane.
	$\|z_0\| \leq 75$ cm	Track displacement along the beam axis from the interaction point.
Good barrel cluster	$N_{blocks} \geq 1$	Number of lead glass blocks in cluster.
	$E_{clusters} \geq 0.1$ GeV	Total energy in cluster.
Good endcap cluster	$N_{blocks} \geq 2$	Number of lead glass blocks in cluster.
	$E_{clusters} \geq 0.2$ GeV	Total energy in cluster.
	$F_{Eblock} \leq 0.99$	Fraction of cluster energy in most energetic block.

Table 4.2: Good track and electromagnetic cluster definitions for the $\tau^+\tau^-$ selection.

The $\tau^+\tau^-$ selection requires that an event have exactly two jets as defined by the following cone algorithm [25]. The jet direction is initially set to the direction of the highest energy good track or electromagnetic cluster in the event, and a cone with a half-angle of 35° is defined about this jet direction. The next highest energy track or cluster within this cone is then added to the jet, and the jet direction is redefined as the vector sum given by the initial jet direction and that of the newly added track or cluster. Once all of the good tracks and clusters that lie within the jet cone have been added, the algorithm begins again with the highest energy track or cluster outside of the cone, and forms another jet cone. This procedure is continued until all of the tracks and clusters in the event are assigned to a cone. Each jet must have at least

one track.

4.3.1 Fiducial requirements

The average $|\cos\theta|$ of the two jets was required to be less than 0.91, in order to avoid using regions of the detector that are not well understood, such as the hadronic pole tips which extend beyond the hadronic endcaps. In addition, three fiducial cuts[2] were applied to restrict the events to regions of the detector which are fully instrumented and which are reasonably well-modelled by the Monte Carlo simulations.

The outer layers of the hadronic calorimeter are used to identify muons in the $\tau^+\tau^-$ selection, and therefore gaps in the hadronic calorimeter will result in more background events entering the $\tau^+\tau^-$ sample. If the direction of the highest momentum track in the jet was extrapolated to a region of the detector associated with gaps between hadronic calorimeter sectors, the entire event was removed from the $\tau^+\tau^-$ sample. The quantity $\phi_{\rm hcal}$ measures the position of a jet relative to the edge of a sector. It is defined as the ϕ position of the highest momentum track in the jet at a radial distance corresponding to the front face of the barrel hadronic calorimeter, modulo 15°. This is shown in Figure 4.1, where it is required that the particle leaves signal in the hadronic calorimeter, and penetrates through to the muon chambers. The fiducial cuts remove the region between the vertical lines in Figure 4.1.

If the direction determined by the jet axis was extrapolated to a region where there are no muon chambers due to the presence of cables or support structures, the entire event was removed from the $\tau^+\tau^-$ sample. These regions are described in detail in Appendix A.

In regions near the anode wire planes in the central drift tracking chamber, par-

[2]A "cut" is a criterion placed upon a variable which removes specific events from the sample.

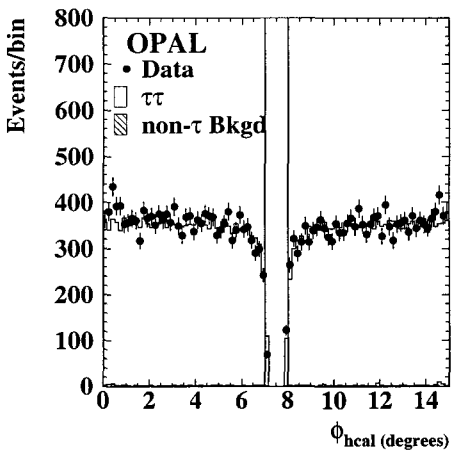

Figure 4.1: ϕ_{hcal}: the ϕ position of a track relative to the HCAL sectors. The value of ϕ_{hcal} has been shifted so that the edges of the sectors are plotted in the centre of the figure. The region between the vertical lines is removed by the fiducial cuts. The points are data, the clear histogram is the Monte Carlo $e^+e^- \to \tau^+\tau^-$ prediction, and the singly-hatched histogram is the Monte Carlo prediction for backgrounds from non-τ sources.

ticles may have their momentum incorrectly reconstructed, an effect that is not well-modelled by the Monte Carlo simulations. The $\tau^+\tau^-$ selection relies on momentum information to identify dimuon events ($e^+e^- \to \mu^+\mu^-$), leading to an excess of dimuon background events in the data. The quantity ϕ_{anode} measures the position of a track relative to the nearest tracking chamber anode plane. It is defined to be the ϕ position of a track extrapolated to the front face of the electromagnetic calorimeter, modulo 15° and shifted so that the anode plane lies at 0°, then weighted by the charge of the track: $\phi_{\text{anode}} = q \times (\text{mod}(\phi_{\text{track}}, 15°) - 7.5°)$. Tracks crossing the anode plane will tend to curve towards negative values of ϕ_{anode} and so an asymmetric cut is applied to this quantity, as shown in Figure 4.2. The track resolution worsens at approximately $\overline{|\cos\theta|} = 0.8$ due to the fact that at smaller θ a particle will pass fewer wires in the tracking jet chamber; therefore, different fiducial cuts are used for $\overline{|\cos\theta|} < 0.8$ and

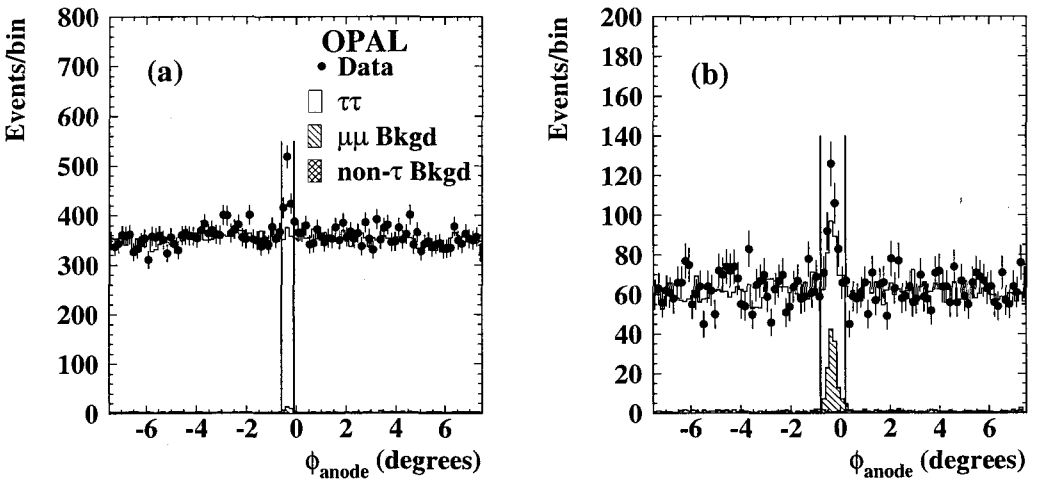

Figure 4.2: ϕ_{anode}: the ϕ position of a track relative to the anode plane regions for (a) $|\cos\theta| < 0.8$, and (b)$|\cos\theta| > 0.8$. The points are data, the clear histogram is the Monte Carlo $e^+e^- \to \tau^+\tau^-$ prediction, the singly-hatched histogram is the Monte Carlo prediction for $e^+e^- \to \mu^+\mu^-$ background, and the doubly-hatched histogram is the Monte Carlo prediction for other types of non-τ background.

$\overline{|\cos\theta|} > 0.8$. In order to enhance the dimuon background, jets which have penetrated into the muon chambers are shown. The excess of data at $\phi_{\text{anode}} = 0°$ is clearly visible. The regions between the two vertical lines are removed by the fiducial cuts.

4.3.2 The selection of $e^+e^- \to \tau^+\tau^-$ events

The main sources of background to the $\tau^+\tau^-$ selection are Bhabha, dimuon, multihadron, and two-photon events. (See Figure 4.3). The identification of each of these backgrounds is discussed below.

Bhabha events, $e^+e^- \to e^+e^-$, have two-particle final states and thus can mimic $\tau^+\tau^-$ events. They are characterized by two high-momentum tracks and large energy deposition in the electromagnetic calorimeter. The criteria used to reject the Bhabha background are identical to those used in the OPAL Z^0 lineshape analysis [26]. The

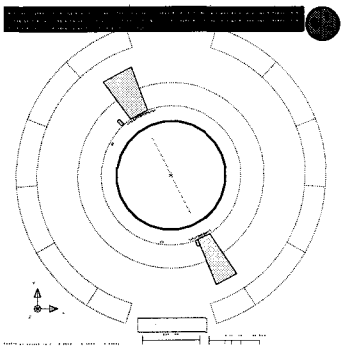

$e^+e^- \rightarrow e^+e^-$

-identified by high reconstructed energy in CTRK and ECAL

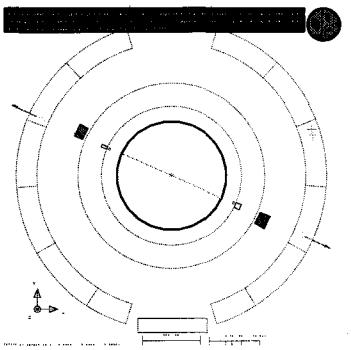

$e^+e^- \rightarrow \mu^+\mu^-$

-identified by high reconstructed energy in CTRK and signal in the outer detectors

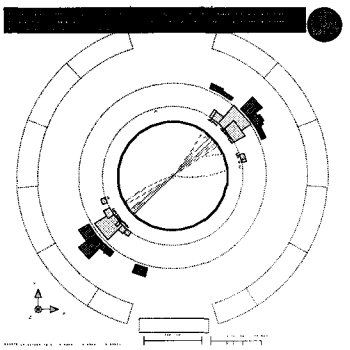

$e^+e^- \rightarrow q\bar{q}$

-identified by high track and cluster multiplicity

Figure 4.3: OPAL background events in the $\tau^+\tau^-$ sample. The view is along the beam direction, showing the transverse plane. The concentric rings correspond to the outer edges of the tracking jet chamber, presampler, electromagnetic calorimeter, hadronic calorimeter, and muon chambers. The rectangles in the electromagnetic and hadronic calorimeters represent energy deposits with the rectangle height being proportional to the amount of energy deposited. The arrows in the central figure correspond to reconstructed tracks in the muon chambers (muon segments).

requirements are different for barrel and endcap regions. The barrel region is defined by $\overline{|\cos\theta|} > 0.70$, and the endcap region by $0.70 < \overline{|\cos\theta|} < 0.91$, where $\overline{|\cos\theta|}$ is the average $|\cos\theta|$ of the two jets. In the barrel region, the lineshape analysis requrement is given by $R_{\rm shw} \leq 0.80$, where $R_{\rm shw}$ is the sum of the energies of all the electromagnetic calorimeter clusters normalized to the centre-of-mass energy. The requirement $R_{\rm vis} \leq 1.4$ was also added in this analysis to further reduce the Bhabha background, where $R_{\rm vis} \equiv R_{\rm shw} + R_{\rm tk}$ and $R_{\rm tk}$ is the scalar sum of the momenta of all the tracks normalized to the centre-of-mass energy. These criteria remove the events above the solid lines in Figure 4.4. In the endcap region, the selection criteria are given by: $R_{\rm shw} \leq 0.80$ for $R_{\rm tk} \leq 0.25$; $R_{\rm vis} \leq 1.05$ for $0.25 < R_{\rm tk} < 0.80$; and $R_{\rm shw} \leq 0.25$ for $R_{\rm tk} > 0.80$. These criteria remove the events above the solid lines in Figure 4.5. The $\tau^+\tau^-$ selection criteria are summarized in Table 4.3.

Dimuon events, $e^+e^- \rightarrow \mu^+\mu^-$, also have two particle final states with high momentum tracks, but little energy deposition in the electromagnetic calorimeter. Dimuon events are removed from the $\tau^+\tau^-$ sample by requiring $R_{\rm vis} \leq 0.60$ in cases where both jets exhibit muon characteristics. A jet may be identified as a muon in the electromagnetic calorimeter by having less than 2.0 GeV of energy deposition; or in the hadronic calorimeter by depositing energy in at least four layers, including at least three of the outermost layers, with fewer than two hits[3] in each layer; or in the muon chambers by leaving a signal in at least two layers. The requirement on $R_{\rm vis}$ prevents those $\tau^+\tau^-$ events from being removed where each τ has decayed via the channel $\tau^- \rightarrow \mu^-\bar{\nu}_\mu\nu_\tau$.

At LEP1 energies, multihadron events, $e^+e^- \rightarrow q\bar{q}$, typically have considerably higher multiplicities than $\tau^+\tau^-$ events, and are removed from the $\tau^+\tau^-$ sample by

[3]A "hit" is a region of energy deposition or signal in the detector.

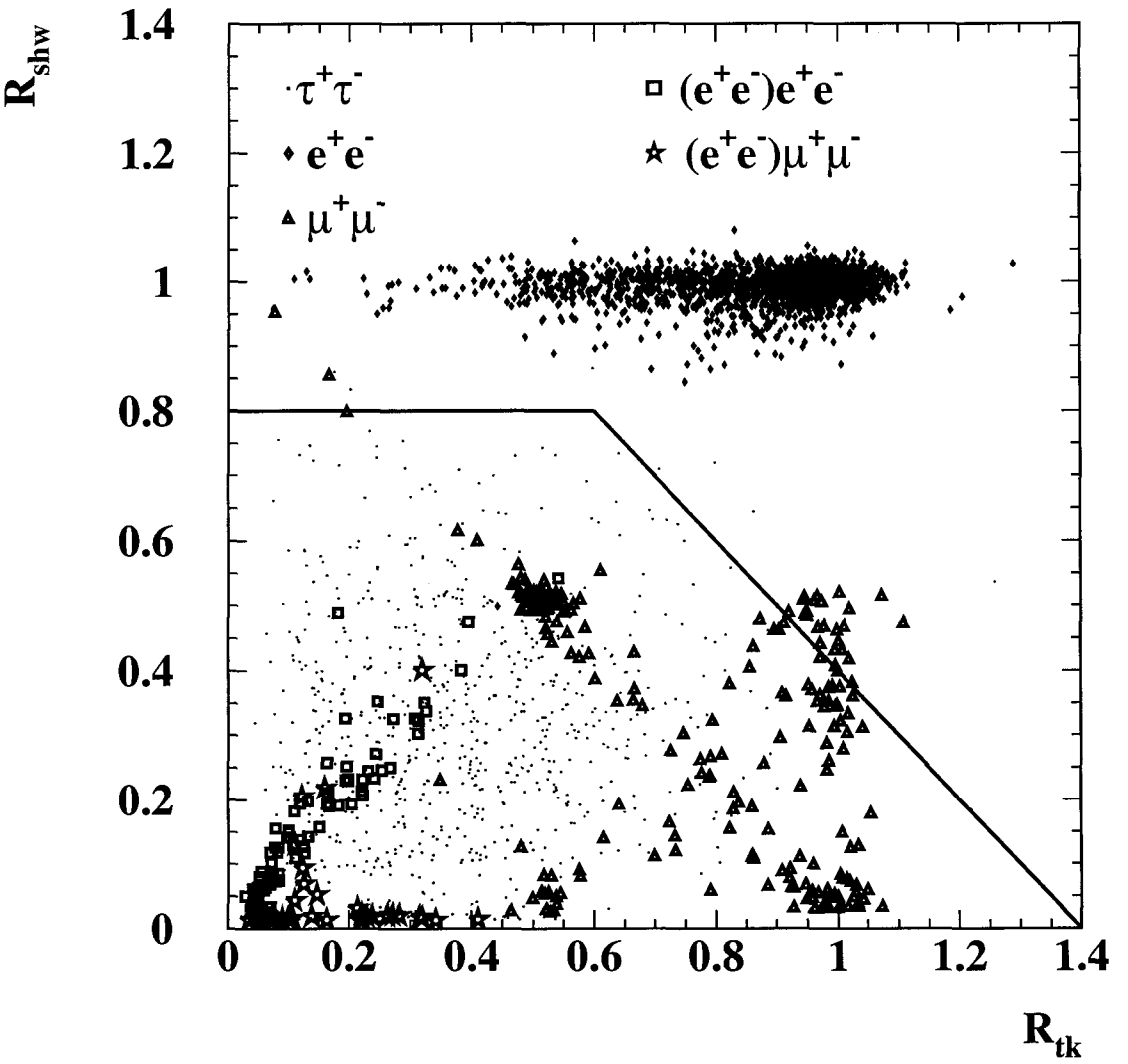

Figure 4.4: Types of background in the $\tau^+\tau^-$ pair sample in the barrel region. Events above the solid lines are rejected by the $\tau^+\tau^-$ selection in order to remove $e^+e^- \rightarrow e^+e^-$ events.

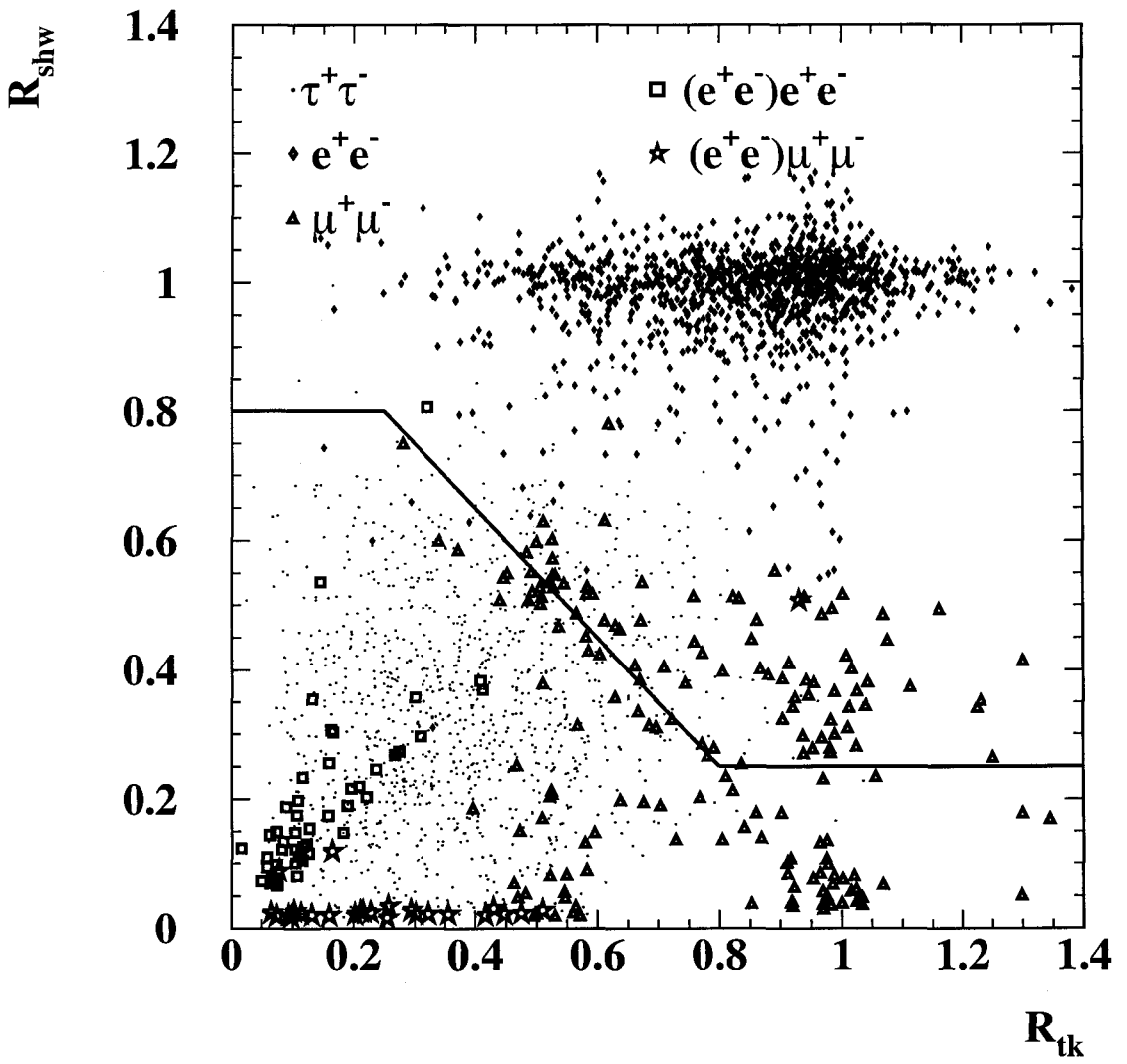

Figure 4.5: Types of background in the $\tau^+\tau^-$ pair sample in the endcap region. Events above the solid lines are rejected by the $\tau^+\tau^-$ selection in order to remove $e^+e^- \rightarrow e^+e^-$ events.

requiring low track and cluster multiplicities: $2 < N_{\rm tks} < 6$ and $N_{\rm cl}^{\rm ecal} \leq 10$, where $N_{\rm tks}$ and $N_{\rm cl}^{\rm ecal}$ are the number of good tracks and electromagnetic clusters in the event.

In two-photon events, $e^+e^- \rightarrow (e^+e^-)\ f\bar{f}$, the incident positron and electron in the beam scatter off each other, interacting via a pair of photons, resulting in the production of an extra pair of fermions. The final state e^+e^- pair has a small scattering angle and disappears down the beam pipe, leaving a pair of low energy fermions, usually $\mu^+\mu^-$ or e^+e^-, in the detector[4]. Since these particles are not produced in the centre-of-mass frame, they are not constrained to be emitted back-to-back. The $\tau^+\tau^-$ selection rejects them based upon their low energy and relatively high acollinearity, $\theta_{\rm acol}$[5].

Cosmic ray events are rejected by using time-of-flight information, and by imposing requirements on the point of closest approach between the reconstructed track and the nominal interaction point in the $r-\phi$ plane ($|d_0|_{\rm min}$) and in the z direction ($|z_0|_{\rm min}$). All of the $\tau^+\tau^-$ selection requirements are given in Table 4.3.

4.4 Backgrounds in the $\tau^+\tau^-$ sample

For each type of background remaining in the $\tau^+\tau^-$ sample, a variable was chosen in which the signal and background can be visibly distinguished. The relative proportion of background was enhanced by modifying the selection criteria. A comparison of the data and Monte Carlo distribution in a background-rich region was then used to assess the modelling of the background and to estimate the corresponding systematic error on the branching ratio. The Monte Carlo simulation provides the overall

[4]Two-photon events with τ particles, $e^+e^- \rightarrow (e^+e^-)\ \tau^+\tau^-$, are considered to be signal.

[5]Acollinearity is the supplement of the angle between the two jets.

Selection	Requirement	Description
Good event	$N_{\rm jet} = 2$	Number of good jets.
	$E_{\rm jet} \geq 0.01 E_{\rm beam}$	Energy of tracks and clusters.
		$E_{\rm beam}$ = Energy of the beam.
	$\overline{\lvert\cos\theta\rvert} < 0.91$	Average $\lvert\cos\theta\rvert$ of the jets.
$e^+e^- \to e^+e^-$	$R_{\rm shw} \leq 0.80$ and $R_{\rm vis} \leq 1.4$	Barrel region.
rejection	$R_{\rm shw} \leq 0.80$	Endcap region: for $R_{\rm tk} < 0.25$,
	$R_{\rm vis} \leq 1.05$	for $0.25 < R_{\rm tk} < 0.80$,
	$R_{\rm shw} \leq 0.25$	and for $R_{\rm tk} > 0.80$.
$e^+e^- \to \mu^+\mu^-$	$R_{\rm vis} \leq 0.6$	if both jets originate from μ's.
rejection	μ's satisfy at least one of:	
	$E_{\rm cl} < 2$ GeV	Energy of the cluster associated
		to the track.
	$N_{\rm hcal} \geq 4$, $N_{\rm hcal}^{\rm outer3} \geq 1$,	Num. of hadronic calorimeter
	and $N_{\rm hits/layer} < 2.0$	hit layers, num. of outer layers
		with hits, average hits per layer.
	$N_{\rm muon} \geq 2$	Num. of muon chamber hit layers.
$e^+e^- \to q\bar{q}$	$2 \leq N_{\rm tks} \leq 6$	Num. of good tracks in event.
rejection	$N_{\rm cl}^{\rm ecal} \leq 10$	Num. of good clusters in event.
Two-photon	$\theta_{\rm acol} \leq 15^\circ$	
rejection	$E_{\rm max} \geq 0.03 E_{\rm cm}$	$E_{\rm max} = \sum_{\rm jets}$ Max $(E_{\rm ecal}, E_{\rm tracks})$.
	and at least one of:	
	$E_{\rm max} > 0.20 E_{CM}$,	
	$E_{\rm ecal} > 2.0$ GeV,	Total cluster energy
	and $E_{\rm tracks} > 2.0$ GeV	and total track energy.
	$\lvert d_0\rvert_{\rm min} \leq 0.5$ cm	Minimum $\lvert d_0\rvert$ of all tracks.
Cosmic ray	$\lvert z_0\rvert_{\rm min} \leq 20.0$ cm	Minimum $\lvert z_0\rvert$ of all tracks.
rejection	$\lvert z_0\rvert_{\rm average} \leq 20.0$ cm	Average $\lvert z_0\rvert$ of all tracks.
	$\lvert t_{\rm meas} - t_{\rm exp}\rvert \leq 10$ ns	for at least one TOF counter.
	$\lvert t_{\rm i} - t_{\rm j}\rvert < 10$ ns	for some TOF counters i and j
		with $\lvert\phi_i - \phi_j\rvert \geq 165^\circ$.

Table 4.3: The τ selection list of criteria.

shape of the background distribution, while the normalization is measured from the data. In most cases, the Monte Carlo simulation was found to be consistent with the data. When the data and Monte Carlo distributions did not agree, the normalization of the Monte Carlo simulation was adjusted to fit the data. Uncertainties of 4% to 20% in the background estimates were obtained from the statistical uncertainty in the normalization, including the Monte Carlo statistical error. The fitting routine is discussed more fully in Appendix B. The following paragraphs discuss the measurement of each type of background in the $\tau^+\tau^-$ sample. Plots of each type of background in the background-enhanced samples are shown, but plots of the unenhanced backgrounds are not shown because, as is evident at the end of the chapter, the total background is very small.

The Bhabha background remaining in the $\tau^+\tau^-$ sample was measured by comparing the distributions of total scalar momentum and of total energy deposition between the data and the Monte Carlo simulation, where the Bhabha background has been enhanced by relaxing the criteria on $R_{\rm vis}$ and $R_{\rm shw}$. The barrel region plot in Figure 4.4 shows that $R_{\rm tk}$ is divided into two regions, $R_{\rm tk} < 0.60$ and $R_{\rm tk} > 0.60$, while the endcap region plot in Figure 4.5 shows that $R_{\rm tk}$ is divided into three regions: $R_{\rm tk} < 0.25$, $0.25 < R_{\rm tk} < 0.80$, and $R_{\rm tk} > 0.80$. Thus, the plots are divided into five regions, two in the barrel and three in the endcap, given by:

1. $\overline{|\cos\theta|} < 0.70$ and $R_{\rm tk} < 0.60$.

2. $\overline{|\cos\theta|} < 0.70$ and $R_{\rm tk} > 0.60$.

3. $\overline{|\cos\theta|} > 0.70$ and $R_{\rm tk} < 0.25$.

4. $\overline{|\cos\theta|} > 0.70$ and $0.25 < R_{\rm tk} < 0.80$.

5. $\overline{|\cos\theta|} > 0.70$ and $R_{\rm tk} > 0.80$.

The Monte Carlo modelling was assessed independently in each of these regions. Figure 4.6 shows the Bhabha background in each of these five regions after normalization factors of 1.2 ± 0.2 (barrel region) and 2.0 ± 0.2 (endcap region) are applied, where Figure 4.6 (a) is region 1 and Figure 4.6 (e) is region 5 as defined above. The arrows in the figures indicate the intervals that were used to determine the normalization factors. The data is well-modelled by the Monte Carlo simulation in the vicinity of the $\tau^+\tau^-$ selection cuts at:

1. $R_{\rm shw} = 0.80$
2. $R_{\rm vis} = 1.4$
3. $R_{\rm shw} = 0.80$
4. $R_{\rm vis} = 1.05$
5. $R_{\rm shw} = 0.25$

for regions 1 to 5, respectively. Region 5 has too few Bhabha events in the vicinity of the cut to determine a normalization factor, and therefore there are no arrows in Figure 4.6 (e). In regions 1 and 2, and in regions 3 and 4, the normalization factors were consistent so that only one normalization factor was applied for the barrel regions and one for the endcap regions. The Bhabha events are not well-modelled but are removed by the $\tau^+\tau^-$ selection. The probability of obtaining a χ^2 value for the fit equal to or greater than those obtained in these fits, $P(\chi^2)$, is 0.000587, 5.48×10^{-8}, $1,45 \times 10^{-5}$, and 0.0833 for regions 1 through 4, respectively. The poor probability for some of these regions reflects the fact that, with high statistics, even small modelling

discrepancies become significant. In each case in this analysis where $P(\chi^2) < 0.01$, the scaling factor and its uncertainty were checked by increasing the errors used in the fitting routine in such a way as to make $P(\chi^2) \approx 0.5$, or χ^2 per degree of freedom = 1. Then, the fit was performed again and the resulting scaling factor and its associated error were compared with the value used in this work. In each case, the change in the value of the scaling factor was negligible, and the uncertainty was less than or equal to the uncertainty already assigned in this work. The fraction of residual Bhabha background in the $\tau^+\tau^-$ sample was then estimated to be 0.00305 ± 0.00027.

The dimuon background remaining after the $\tau^+\tau^-$ selection was determined by measuring the dimuon contribution to the scalar momentum distribution in the data and in the Monte Carlo simulation, where the dimuon background has been enhanced by relaxing the criterion on $R_{\rm vis}$ and by requiring at least three hit layers of muon chambers and exactly one good track in each jet. At least one of the jets must have a track reconstructed in the muon chambers which matches well with the good track reconstructed in the central tracking chamber. Figure 4.7 (a) shows the dimuon background in this sample. The normalization factor was found to be 1.0 ± 0.2 with $P(\chi^2) = 0.0189$, and the fractional background in the $\tau^+\tau^-$ sample was estimated to be 0.00108 ± 0.00022.

The τ jets are typically much more collimated than multihadron jets. The distribution of the maximum angle between any good track in the hemisphere and the jet direction was used to evaluate the agreement between the data and the Monte Carlo modelling of these events, where the multihadron background has been enhanced by relaxing the multiplicity criteria in the $\tau^+\tau^-$ selection, and then requiring at least four tracks in the event. Figure 4.7 (b) shows the multihadron background in this background-enhanced sample, which has $P(\chi^2) = 3.25 \times 10^{-7}$. A scaling factor

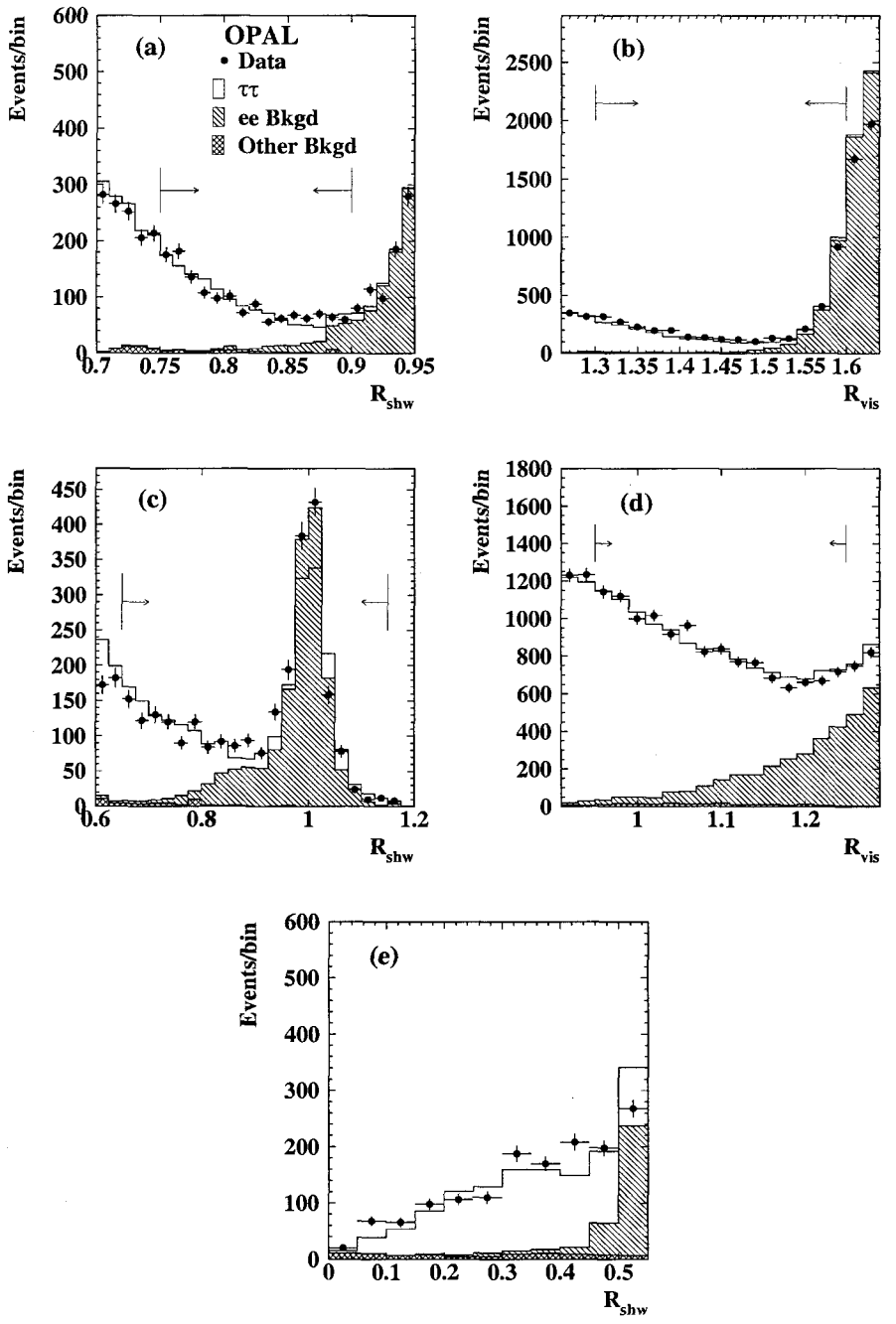

Figure 4.6: $e^+e^- \rightarrow e^+e^-$ background in the $\tau^+\tau^-$ sample for (a) region 1, (b) region 2, (c) region 3, (d) region 4, and (e) region 5. The points are data, the clear histogram is the Monte Carlo $e^+e^- \rightarrow \tau^+\tau^-$ prediction, the singly-hatched histogram is the Monte Carlo $e^+e^- \rightarrow e^+e^-$ prediction, and the cross-hatched histogram is the Monte Carlo prediction for all other types of background.

of 0.49 ± 0.02 was applied to the multihadron background, resulting in a fractional background estimate of 0.00377 ± 0.00015. This scaling factor is significantly less than unity because the multihadron Monte Carlo simulations overestimate the number of low multiplicity events as compared with the data.

The acollinearity criterion was relaxed in order to enhance the two-photon background so that it could be measured. In addition, for $e^+e^- \rightarrow (e^+e^-)\ \mu^+\mu^-$ events, each jet was required to exhibit muon characteristics, while for $e^+e^- \rightarrow (e^+e^-)\ e^+e^-$ events, each jet was required to exhibit electron characteristics. The muon characteristics were: exactly one track in each jet; at least two muon hit layers in each jet, at least one set of which must match well with the corresponding track; and $R_{\rm tk} < 0.5$. The comparison between data and Monte Carlo simulation for this sample is shown in Figure 4.7 (c), and led to a scaling factor of 1.0 ± 0.5, a probability of $P(\chi^2) = 0.000593$, and a fractional background estimate of 0.00108 ± 0.00054 for the $e^+e^- \rightarrow (e^+e^-)\ \mu^+\mu^-$ background in the $\tau^+\tau^-$ sample. The electron characteristics were: exactly one track in each jet; no muon hit layers in either jet; $9 < dE/dx < 11$ in each jet; $E_{\rm ecal}/p_{\rm tks} > 0.7$, where $E_{\rm ecal}$ is the jet energy measured in the electromagnetic calorimeter and $p_{\rm tks}$ is the jet momentum measured in the tracking chamber; and $R_{\rm shw} < 0.4$. The comparison between data and Monte Carlo simulation for this sample is shown in Figure 4.7 (d), and led to a scaling factor of 1.2 ± 0.2, a probability of $P(\chi^2) = 0.925$, and a fractional background estimate of 0.00157 ± 0.00028 for the $e^+e^- \rightarrow (e^+e^-)\ e^+e^-$ background in the $\tau^+\tau^-$ sample.

The $\tau^+\tau^-$ selection leaves a sample of 96,898 candidate $\tau^+\tau^-$ events, with a predicted fractional background of 0.01055 ± 0.00072. The backgrounds in the $\tau^+\tau^-$ sample are summarized in Table 4.4.

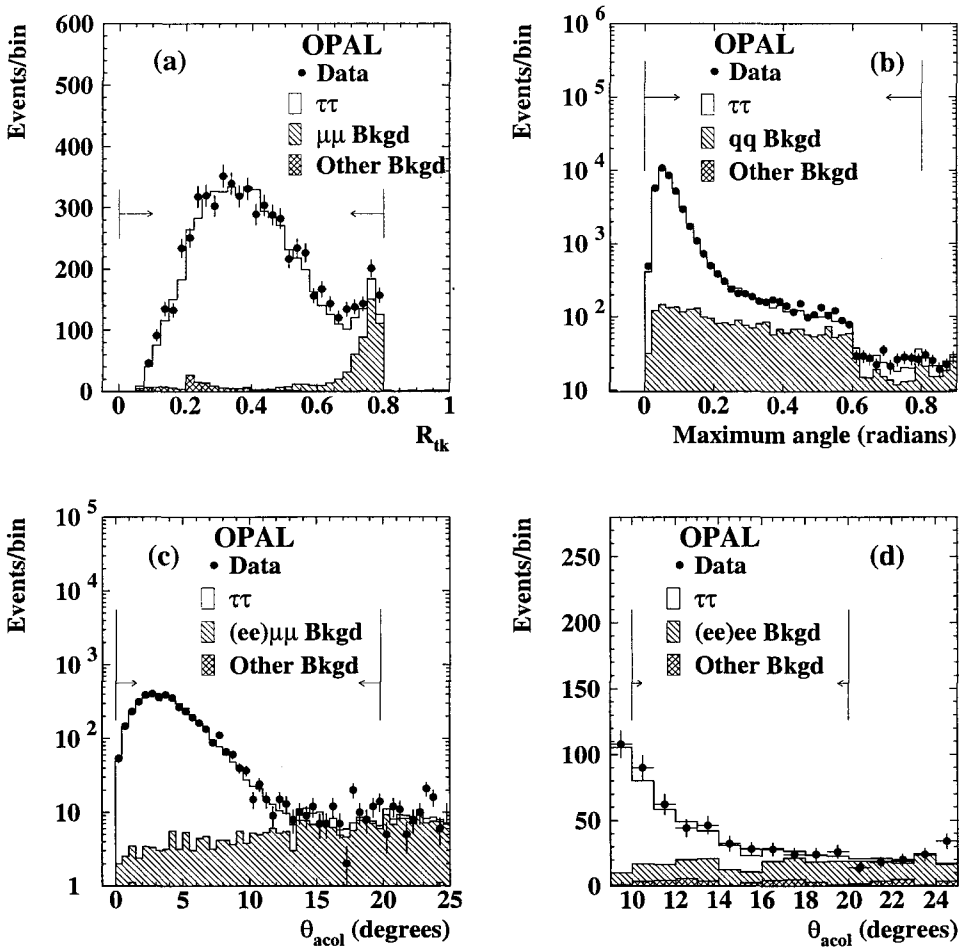

Figure 4.7: The distributions used to measure backgrounds in the $\tau^+\tau^-$ sample are shown after normalization. (a) $R_{\rm tk}$ is the energy measured in the tracking chamber, (b)the maximum angle between any good track and the jet direction, and (c, d) $\theta_{\rm acol}$ is the acollinearity angle between the two τ jets. The points are data, the clear histogram is the Monte Carlo $e^+e^- \to \tau^+\tau^-$ prediction, the singly-hatched histogram is the Monte Carlo prediction for the type of background being evaluated using each distribution, and the cross-hatched histogram is the Monte Carlo prediction for all other types of background.

Background	Contamination
$e^+e^- \to e^+e^-$	0.00305 ± 0.00027
$e^+e^- \to \mu^+\mu^-$	0.00108 ± 0.00022
$e^+e^- \to q\bar{q}$	0.00377 ± 0.00015
$e^+e^- \to (e^+e^-)\ \mu^+\mu^-$	0.00108 ± 0.00054
$e^+e^- \to (e^+e^-)\ e^+e^-$	0.00157 ± 0.00028
Total	0.01055 ± 0.00072

Table 4.4: Fractional backgrounds in the $\tau^+\tau^-$ sample together with their estimated uncertainties.

Chapter 5

The selection of $\tau^- \rightarrow \mu^- \bar{\nu}_\mu \nu_\tau$ jets

After the $\tau^+\tau^-$ selection, each of the 193,796 candidate τ jets ($= 96,898 \times 2$) is analysed individually to see whether it exhibits the characteristics of the required $\tau^- \rightarrow \mu^- \bar{\nu}_\mu \nu_\tau$ signature. Figure 5.1 shows a $\tau^+\tau^-$ event in which one τ has decayed to a muon and neutrinos, and the other τ has decayed to a meson which subsequently decays to a neutral and a charged pion. A muon from a τ decay will result in a track in the central tracking chamber, little energy in the electromagnetic and hadronic calorimeters, and a track in the muon chambers. The $\tau^- \rightarrow \mu^- \bar{\nu}_\mu \nu_\tau$ selection is based on information from the central tracking chamber and the muon chambers. Calorimeter information is not used in the main selection, but instead is used to create an independent $\tau^- \rightarrow \mu^- \bar{\nu}_\mu \nu_\tau$ control sample that is used to estimate the systematic error in the selection efficiency. The branching ratio of the $\tau^- \rightarrow \mu^- \bar{\nu}_\mu \nu_\tau$ decay is inclusive of radiation in the initial or final state [1], and so the $\tau^- \rightarrow \mu^- \bar{\nu}_\mu \nu_\tau$ selection retains decays that are accompanied by a radiative photon or a radiative photon that has converted in the detector into an e^+e^- pair.

The $\tau^- \rightarrow \mu^- \bar{\nu}_\mu \nu_\tau$ candidates are selected from jets with one to three tracks in the tracking chamber, where the tracks are ordered according to decreasing particle momentum. In order to be a muon candidate, evidence is required that the highest

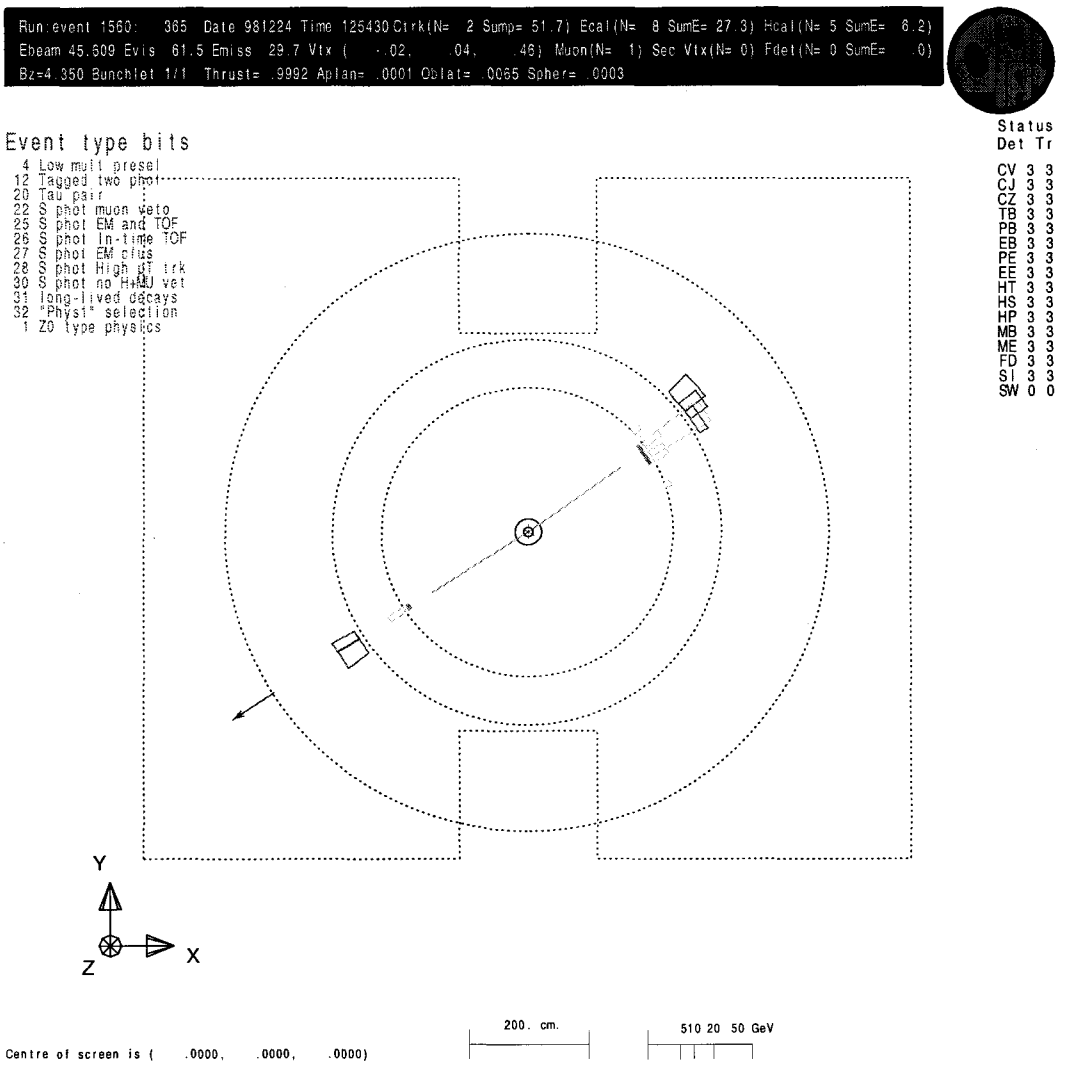

Figure 5.1: A Monte Carlo simulation of a $\tau^+\tau^-$ event in the OPAL detector, where one τ has decayed via $\tau^- \to \mu^- \bar{\nu}_\mu \nu_\tau$ and the other τ has decayed to a meson which subsequently decays to $\pi\pi^0$. The concentric rings correspond to the outer edges of the beam pipe, tracking jet chamber, electromagnetic calorimeter, and hadronic calorimeter. The arrow indicates a reconstructed track in the muon chambers.

momentum track in the tracking chamber is well aligned with a track in the muon chambers.

Tracks in the muon chambers are reconstructed independently from those in the tracking chamber, and require at least three hits in the muon chambers, and a perpendicular distance from the track to the vertex of less than 400 cm.

In $\tau^- \to \mu^- \bar{\nu}_\mu \nu_\tau$ decays, the highest momentum track in the tracking chamber is typically well-aligned with the corresponding track in the muon chambers, whereas this is not the case for hadronic τ decays, which are the main source of background in the sample. The majority of these background jets contain a pion which interacts in the hadronic calorimeter, resulting in the production of secondary particles which emerge from the calorimeter and generate signals in the muon chambers, a process known as pion punchthrough. Therefore, a "muon matching" variable, $\mu_{\rm match}$, which compares the agreement between the direction of a track reconstructed in the tracking chamber and that of the track reconstructed in the muon chambers, is used to differentiate the signal $\tau^- \to \mu^- \bar{\nu}_\mu \nu_\tau$ decays from hadronic τ decays[1]. It is required that $\mu_{\rm match}$ have a value of less than 5, (see Figure 5.2 (a) and (b)). The position of the cut was chosen to minimise the background while retaining signal.

In a few cases, even though a jet passes the $\mu_{\rm match}$ criterion, not all of the muon chamber hits associated with the track in the muon chambers are associated with the track extrapolated from the tracking chamber. Some pions and poorly reconstructed muons are removed by selecting tracks in the tracking chamber that are associated with a signal in at least three muon chamber layers. $N_{\rm muon}$ is the number of muon

[1] $\mu_{\rm match}$ measures the difference in ϕ and in θ between a track reconstructed in the tracking chamber and one reconstructed in the muon chambers, at the radial (z) position corresponding to the front face of the barrel (endcap) muon chambers. The differences are divided by an error estimate and added in quadrature to form a χ^2-like comparison of the directions.

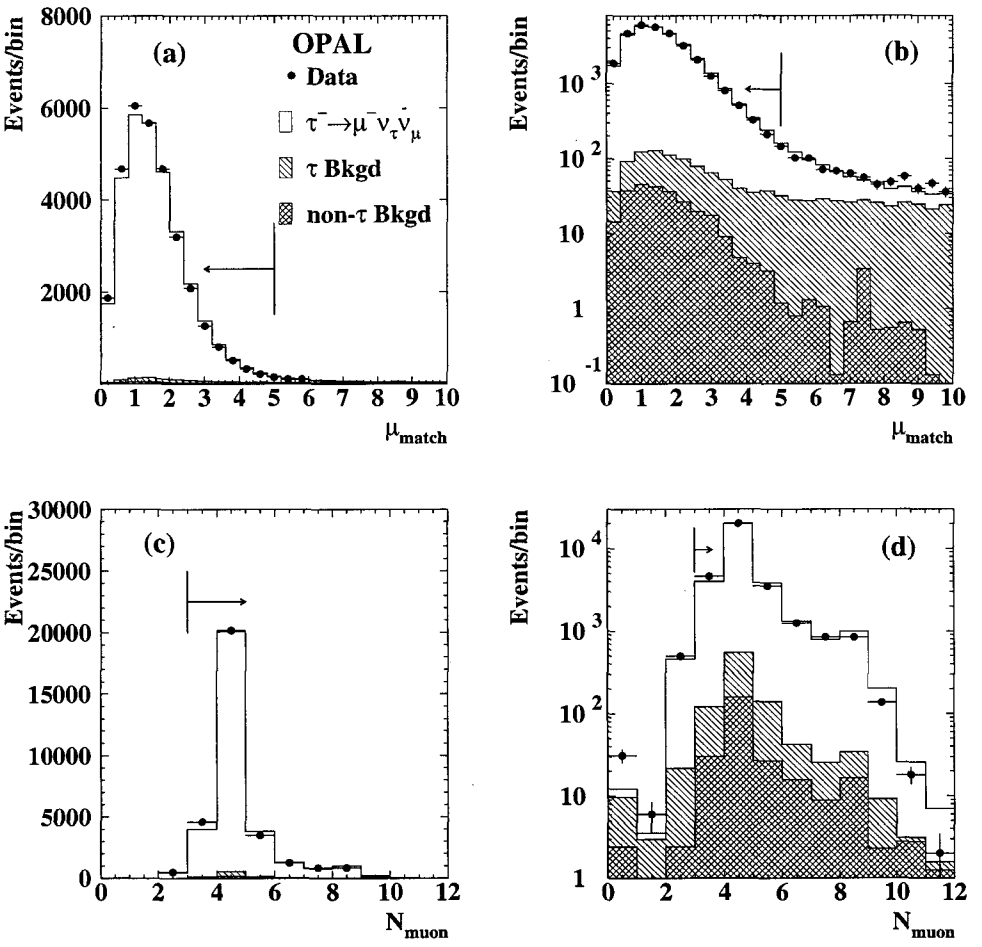

Figure 5.2: (a, b) The μ_{match} matching between a muon track reconstructed in the tracking chamber and one reconstructed in the muon chamber, and (c, d) the number of muon chamber layers, N_{muon}, activated by the passage of a charged particle in the jet. The jets in each plot have passed all other selection criteria. The arrows indicate the accepted regions. The points are data, the clear histogram is the Monte Carlo $\tau^- \to \mu^- \bar{\nu}_\mu \nu_\tau$ prediction, the singly-hatched histogram is the Monte Carlo prediction for backgrounds from other τ decays, and the cross-hatched histogram is the Monte Carlo prediction for background from non-τ sources.

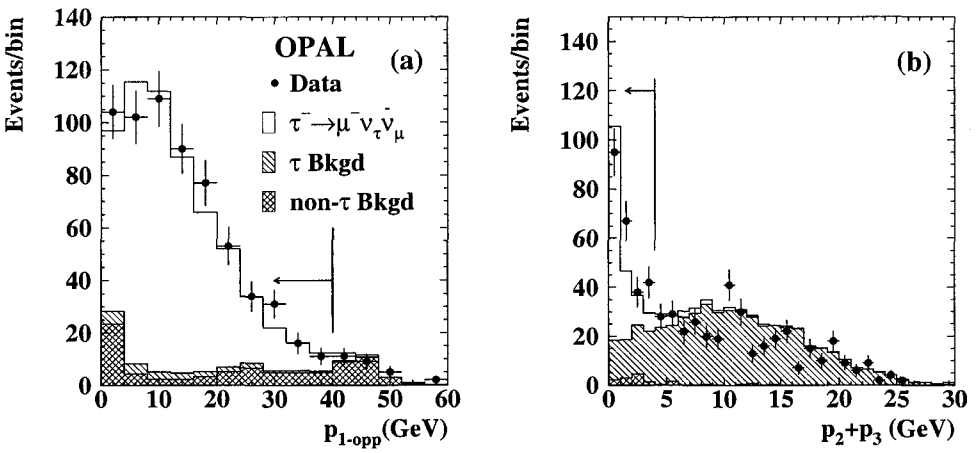

Figure 5.3: (a) The momentum of the highest momentum particle in the opposite jet, $p_{1-\mathrm{opp}}$, where the candidate muon has a momentum greater than 40 GeV, and (b) the combined momentum of the second and third particles in those jets which have more than one track, for jets which have passed all other selection criteria. The arrows indicate the accepted regions.

chamber layers activated by a passing particle, and we require $N_{\mathrm{muon}} > 2$, as shown in Figure 5.2 (c) and (d).

In order to reduce background from dimuon events, it is required that the momentum of the highest momentum particle in at least one of the two jets in the event, i.e. p_1 in the candidate jet and $p_{1-\mathrm{opp}}$ in the opposite jet, must be less than 40 GeV (see Figure 5.3 (a)).

Although the $\tau^- \to \mu^- \bar{\nu}_\mu \nu_\tau$ candidates in general are expected to have one track, in approximately 2% of these decays a radiated photon converts to an e^+e^- pair, resulting in one or two extra tracks in the tracking chamber. In order to retain these jets but eliminate background jets, it is required that the scalar sum of the momenta of the two lower-momentum particles, $p_2 + p_3$, must be less than 4 GeV (see Figure 5.3 (b)). In cases where there is only one extra track, p_3 is taken to be zero.

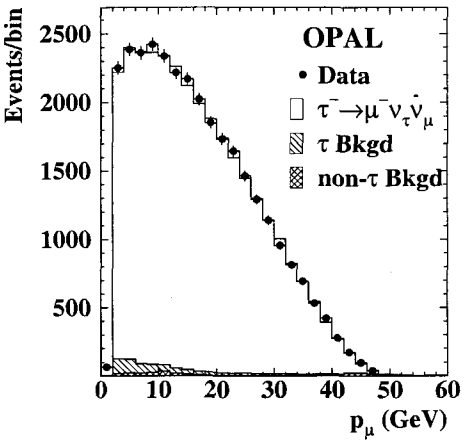

Figure 5.4: The momentum of the candidate muon, p_μ, for jets which have passed all of the selection criteria. No criteria are made on this variable.

The above criteria leave a sample of 31,395 candidate $\tau^- \to \mu^-\bar{\nu}_\mu\nu_\tau$ jets. The quality of the data is illustrated in Figure 5.4, which shows the momentum of the candidate muon for jets which satisfy the $\tau^- \to \mu^-\bar{\nu}_\mu\nu_\tau$ selection. No criteria are made on this variable. The backgrounds remaining in this sample are discussed in the next section.

5.1 Backgrounds in the $\tau^- \to \mu^-\bar{\nu}_\mu\nu_\tau$ sample

The background contamination in the signal $\tau^- \to \mu^-\bar{\nu}_\mu\nu_\tau$ sample stems from other τ decay modes and from residual non-τ background in the $\tau^+\tau^-$ sample. The procedure used to evaluate the background in the $\tau^- \to \mu^-\bar{\nu}_\mu\nu_\tau$ sample is identical to the one used to evaluate the background in the $\tau^+\tau^-$ sample, which is outlined in Section 4.4 and in Appendix B.

The main backgrounds from other τ decay modes can be separated into τ decays involving a single charged hadron, h, which may be a pion, π, kaon, K, or rho meson,

ρ, and a small number of decays involving three charged hadrons. These decays may or may not be accompanied by neutral pions, and are written as $\tau^- \to h^- \geq 0\pi^0 \nu_\tau$ and $\tau^- \to h^- h^- h^+ \geq 0\pi^0 \nu_\tau$. The $\tau^- \to h^- \geq 0\pi^0 \nu_\tau$ decays can pass the $\tau^- \to \mu^- \bar{\nu}_\mu \nu_\tau$ selection when the charged hadron punches through the calorimeters, leaving a signal in the muon chambers. The absence or presence of π^0s has no impact on whether or not the jet is selected, since there are over 60 radiation lengths of material in the detector in front of the muon chambers. The modelling of this background was tested by studying $\tau^- \to \mu^- \bar{\nu}_\mu \nu_\tau$ jets with large deposits of energy in the electromagnetic calorimeter, which led to a scaling factor of 1.00 ± 0.09 and $P(\chi^2) = 0.121$. The distribution of jet energy, $E_{\rm jet}$, deposited in the electromagnetic calorimeter is shown in Figure 5.5 (a). The $\tau^- \to h^- \geq 0\pi^0 \nu_\tau$ fractional background estimate is 0.0225 ± 0.0016, of which approximately 75% includes at least one π^0.

The main backgrounds resulting from contamination in the $\tau^+\tau^-$ sample are $e^+e^- \to (e^+e^-)\, \mu^+\mu^-$ and $e^+e^- \to \mu^+\mu^-$ events. The $e^+e^- \to (e^+e^-)\, \mu^+\mu^-$ contribution in the $\tau^- \to \mu^- \bar{\nu}_\mu \nu_\tau$ sample was evaluated by fitting the Monte Carlo distribution of $\theta_{\rm acol}$ to that of the data, where the acollinearity criterion in the $\tau^+\tau^-$ selection which requires that $\theta_{\rm acol} < 15°$ has been relaxed, and $p_{\rm tot}$ is required to be less than 20 GeV, as shown in Figure 5.5 (b). This resulted in a scaling factor of 1.0 ± 0.5, which is consistent with the scaling factor obtained in Section 4.4, a probability of $P(\chi^2) = 0.561$, and a fractional background estimate of 0.0052 ± 0.0026. For this particular background, the quoted uncertainty also takes into account the spread in the fitted normalization when the range of $\theta_{\rm acol}$ is extended to 20 and to 25 degrees. This is motivated by a discrepancy between the data and the Monte Carlo simulation which can be seen in the region where $\theta_{\rm acol} > 20°$.

The contribution of dimuon events ($e^+e^- \to \mu^+\mu^-$) was enhanced in the $\tau^- \to$

$\mu^- \bar{\nu}_\mu \nu_\tau$ sample by removing the requirement that $p_{1-\mathrm{opp}} < 40$ GeV or $p_1 < 40$ GeV, and instead requiring that $p_1 > 40$ GeV. The distribution of $p_{1-\mathrm{opp}}$ was then used to evaluate the agreement between the data and the Monte Carlo simulation for this background. The resulting scaling factor of 1.0 ± 0.2 is consistent with that obtained in Section 4.4, and the estimate of the dimuon fractional background in the $\tau^- \to \mu^- \bar{\nu}_\mu \nu_\tau$ sample is 0.0029 ± 0.0006. The corresponding distribution is shown in Figure 5.5 (c), and has $\mathrm{P}(\chi^2) = 0.639$.

Signal events with three tracks are due to radiative $\tau^- \to \mu^- \bar{\nu}_\mu \nu_\tau$ decays where the photon converts in the tracking chamber to an $\mathrm{e}^+\mathrm{e}^-$ pair, whereas the three-track background consists mainly of jets with three pions in the final state. Electrons and pions have different rates of energy loss in the OPAL tracking chamber, and hence the background can be isolated from the signal by using the rate of energy loss as the particle traverses the tracking chamber, $\mathrm{d}E/\mathrm{d}x$, of the second-highest-momentum particle in the jet. The Monte Carlo modelling was compared to the data as shown in Figure 5.5 (d), yielding a scaling factor of 1.5 ± 0.3, a probability of $\mathrm{P}(\chi^2) = 0.436$, and a fractional background measurement of 0.0014 ± 0.0003.

The remaining background in the $\tau^- \to \mu^- \bar{\nu}_\mu \nu_\tau$ sample is almost negligible and is estimated from the Monte Carlo simulation. The total estimated fractional background in the $\tau^- \to \mu^- \bar{\nu}_\mu \nu_\tau$ sample after the selection is 0.0324 ± 0.0031. The main background contributions are summarized in Table 5.1.

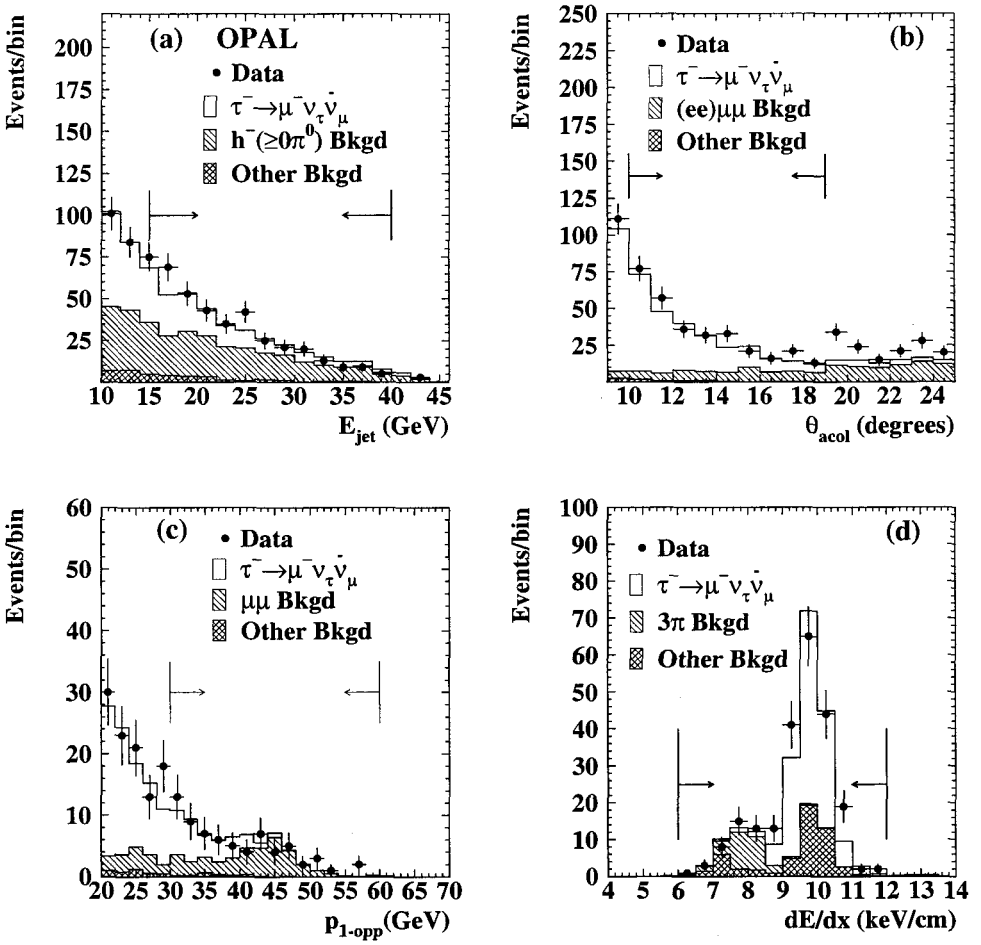

Figure 5.5: The distributions used to measure the background in the $\tau^- \to \mu^- \bar{\nu}_\mu \nu_\tau$ sample are shown after the normalization. The arrows indicate the region that was chosen to measure each background. (a) $E_{\rm jet}$ is the energy measured in the electromagnetic calorimeter, (b) $\theta_{\rm acol}$ is the acollinearity angle between the two τ jets, (c) $p_{1-{\rm opp}}$ is the momentum of the highest momentum particle in the opposite jet to the $\tau^- \to \mu^- \bar{\nu}_\mu \nu_\tau$ candidate, (d) dE/dx is the rate of energy loss of a particle traversing the tracking chamber. The points are data, the clear histogram is the Monte Carlo $\tau^- \to \mu^- \bar{\nu}_\mu \nu_\tau$ prediction, the singly-hatched histogram is the Monte Carlo prediction for the type of background being evaluated using each distribution, and the cross-hatched histogram is the Monte Carlo prediction for all other types of background.

Backgrounds	Contamination
$\tau^- \to h^- \geq 0\pi^0 \nu_\tau$	0.0225 ± 0.0016
$e^+e^- \to (e^+e^-)\ \mu^+\mu^-$	0.0052 ± 0.0026
$e^+e^- \to \mu^+\mu^-$	0.0029 ± 0.0006
$\tau^- \to h^-h^-h^+ \geq 0\pi^0 \nu_\tau$	0.0014 ± 0.0003
Other	0.0004 ± 0.0001
Total	0.0324 ± 0.0031

Table 5.1: The main sources of background in the candidate $\tau^- \to \mu^- \bar{\nu}_\mu \nu_\tau$ sample together with their estimated uncertainties.

Chapter 6

The $\tau^- \to \mu^- \bar{\nu}_\mu \nu_\tau$ branching ratio

The $\tau^- \to \mu^- \bar{\nu}_\mu \nu_\tau$ branching ratio is given by

$$\mathrm{B} = \frac{N_{(\tau\to\mu)}}{N_\tau} \frac{(1 - f_{\mathrm{bk}})}{(1 - f_{\tau\mathrm{bk}})} \frac{1}{\epsilon_{(\tau\to\mu)}} \frac{1}{F_{\mathrm{b}}}, \tag{6.1}$$

where the first term, $N_{(\tau\to\mu)}/N_\tau$, is extracted from the data as the number of $\tau^- \to \mu^- \bar{\nu}_\mu \nu_\tau$ candidates after the $\tau^- \to \mu^- \bar{\nu}_\mu \nu_\tau$ selection, divided by the number of τ candidates selected by the $\tau^+\tau^-$ selection. The remaining terms include the estimated fractional backgrounds in the $\tau^- \to \mu^- \bar{\nu}_\mu \nu_\tau$ and $\tau^+\tau^-$ samples, f_{bk} and $f_{\tau\mathrm{bk}}$, respectively, which must be subtracted off the numerator and denominator in the first term of Equation 6.1. The evaluation of these backgrounds has been discussed in Sections 4.4 and 5.1. The efficiency of selecting the $\tau^- \to \mu^- \bar{\nu}_\mu \nu_\tau$ jets out of the sample of $\tau^+\tau^-$ candidates is given by

$$\epsilon_{(\tau\to\mu)} = \frac{N^{\mathrm{after}}_{(\tau\to\mu)}}{N^{\mathrm{before}}_{(\tau\to\mu)}}, \tag{6.2}$$

where $N^{\mathrm{after}}_{(\tau\to\mu)}$ is the number of $\tau^- \to \mu^- \bar{\nu}_\mu \nu_\tau$ jets in the Monte Carlo simulation after the $\tau^- \to \mu^- \bar{\nu}_\mu \nu_\tau$ selection, and $N^{\mathrm{before}}_{(\tau\to\mu)}$ is the number of $\tau^- \to \mu^- \bar{\nu}_\mu \nu_\tau$ jets in the Monte Carlo simulation before the $\tau^- \to \mu^- \bar{\nu}_\mu \nu_\tau$ selection, but after the $\tau^+\tau^-$ selection. The Monte Carlo prediction of the efficiency is cross-checked using a control sample, and will be discussed in Section 6.1. F_{b} is a bias factor which accounts for

the fact that the $\tau^+\tau^-$ selection does not select all τ decay modes with the same efficiency, and will also be explained in more detail in Section 6.1. The corresponding values of these parameters for the $\tau^- \to \mu^- \bar{\nu}_\mu \nu_\tau$ selection are shown in Table 6.1. Equation 6.1 results in a branching ratio value of

$$\mathrm{B}(\tau^- \to \mu^- \bar{\nu}_\mu \nu_\tau) = 0.1734 \pm 0.0009 \pm 0.0006,$$

where the first error is statistical and the second is systematic. The statistical uncertainty in the branching ratio is taken to be the binomial error in the uncorrected branching ratio, $N_{(\tau\to\mu)}/N_\tau$, and is given by $\sqrt{f(1-f)/N_\tau}$ where $f = N_{(\tau\to\mu)}/N_\tau$.

Parameter	Value
$N_{(\tau\to\mu)}$	31,395
N_τ	193,796
f_{bk}	0.0324 ± 0.0031
$f_{\tau\mathrm{bk}}$	0.0106 ± 0.0007
$\epsilon_{(\tau\to\mu)}$	0.8836 ± 0.0021
F_{b}	1.0339 ± 0.0020
$\mathrm{B}(\tau^- \to \mu^- \bar{\nu}_\mu \nu_\tau)$	$0.1734 \pm 0.0009(stat) \pm 0.0006(syst)$

Table 6.1: Values of the quantities used in the calculation of $\mathrm{B}(\tau^- \to \mu^- \bar{\nu}_\mu \nu_\tau)$.

6.1 Systematic checks

The systematic errors include the contributions associated with the Monte Carlo modelling of each of the main sources of background in the $\tau^- \to \mu^- \bar{\nu}_\mu \nu_\tau$ sample, the error in the efficiency, the error in the background in the $\tau^+\tau^-$ sample, and the error in the bias factor. These errors are listed in Table 6.1 and their contribution to the error in the branching ratio is shown in Table 6.2. The errors in the backgrounds have already been discussed in Sections 4.4 and 5.1. A discussion of the error in the efficiency and in the bias factor follows.

A second sample of $\tau^- \to \mu^- \bar{\nu}_\mu \nu_\tau$ data candidates was selected using information from the tracking chamber plus the electromagnetic and hadronic calorimeters. The selection looks for jets with one to three tracks satisfying $p_2 + p_3 < 4$ GeV that leave little energy in the electromagnetic or hadronic calorimeters but still leave an observable signal in several layers of the hadronic calorimeter. This yields a sample of 28,042 $\tau^- \to \mu^- \bar{\nu}_\mu \nu_\tau$ jets and results in a branching ratio of 0.1730 ± 0.0010 with a measured fractional background of 0.0396 ± 0.0003 and an efficiency of 0.7853 ± 0.0006. The errors on these numbers are statistical only, since a full evaluation of the systematic errors was not carried out as the selection was to be used only as a check. The candidates selected using this *calorimeter* selection are approximately 90% correlated with those selected for the main branching ratio analysis using the *tracking* selection, even though the two selection procedures are largely independent. Because of the high level of correlation, the advantage of combining the two selection methods is negligible; however, the calorimeter selection is very useful for producing a control sample of $\tau^- \to \mu^- \bar{\nu}_\mu \nu_\tau$ jets which can be used for systematic checks.

A potentially important source of systematic error in the analysis is the Monte Carlo modelling of the selection efficiency. In order to estimate the systematic error on the efficiency, both data and Monte Carlo simulated jets are required to satisfy the calorimeter selection criteria. This produces two control samples of candidate $\tau^- \to \mu^- \bar{\nu}_\mu \nu_\tau$ jets, one which is data, and one which is Monte Carlo simulation. The efficiency of the tracking selection is then evaluated as the fraction of jets in the calorimeter sample which pass the tracking selection. The ratio of the efficiency found using the data to the efficiency found using the Monte Carlo simulation is 1.0002 ± 0.0024. The uncertainty in the ratio is calculated by taking the quadrature sum of the binomial errors on the two efficiencies, and is taken as the systematic error

in the $\tau^- \to \mu^- \bar{\nu}_\mu \nu_\tau$ selection efficiency.

Further checks of the Monte Carlo modelling are made by varying each of the selection criteria and noting the resulting changes in the branching ratio. The requirement on the number of tracks was changed to allow only one track in the jet, in order to remove the radiative decays with photon conversions. This was found to change the branching ratio by 0.0003. Changing the requirement on N_{muon} from two to one resulted in a branching ratio change of 0.0002. Removing this criterion entirely resulted in a change of 0.0003. Varying the μ_{match} value of the match between a tracking chamber track and a muon chamber track by $\pm 1/2$ resulted in changes of 0.0002. The requirement on $p_{1-\text{opp}}$ was changed by ± 2 GeV and resulted in a change of 0.00001. Removing the requirement of $p_{1-\text{opp}}$ entirely results in a similar change. All of these changes are within the systematic uncertainty that has already been assigned due to the background and efficiency errors, which are equivalent to an uncertainty in the branching ratio of 0.0005. Thus one has confidence that the error in the modelling of the background and the signal does not exceed the error already quoted.

The τ Monte Carlo simulations create events for the different τ decay modes in accordance with the known measured τ decay branching ratios [1]. However, the $\tau^+\tau^-$ selection does not select each τ decay mode with equal efficiency. This can introduce a bias in the measured value of $\text{B}(\tau^- \to \mu^- \bar{\nu}_\mu \nu_\tau)$. The $\tau^+\tau^-$ selection bias factor, F_{b}, measures the degree to which the $\tau^+\tau^-$ selection favours or suppresses the decay $\tau^- \to \mu^- \bar{\nu}_\mu \nu_\tau$ relative to other τ decay modes. It is defined as the ratio of the fraction of $\tau^- \to \mu^- \bar{\nu}_\mu \nu_\tau$ decays in a sample of τ decays after the $\tau^+\tau^-$ selection is applied, to the fraction of $\tau^- \to \mu^- \bar{\nu}_\mu \nu_\tau$ decays before the selection. The dependence of the bias factor on $\text{B}(\tau^- \to \mu^- \bar{\nu}_\mu \nu_\tau)$ was checked by varying the branching ratio within the

uncertainty of 0.0007 given in reference [1]. This resulted in negligible changes in the bias factor. In addition, extensive studies of systematic errors in the bias factor have been made in previous OPAL τ-decay analyses [27, 28], including rescaling the centre-of-mass energy and then recalculating the bias factor, and smearing some Monte Carlo variables and then again recalculating the bias factor. These checks have indicated that the systematic effects do not contribute to the uncertainty in a significant manner compared with the statistical uncertainty, and so we have not included a systematic component in the error.

Source	Absolute error
$\epsilon_{(\tau\to\mu)}$	0.00040
F_{b}	0.00034
f_{bk}	0.00030
$f_{\tau\mathrm{bk}}$	0.00012
Total	0.00062

Table 6.2: Contributions to the total branching ratio absolute systematic uncertainty. The uncertainty in f_{bk} has been adjusted to take into account correlations between the backgrounds in the $\tau^+\tau^-$ and $\tau^- \to \mu^- \bar{\nu}_\mu \nu_\tau$ samples, as detailed in Appendix C.

Chapter 7

Discussion

The value of $B(\tau^- \rightarrow \mu^- \bar{\nu}_\mu \nu_\tau)$ obtained in this analysis can be used in conjunction with the previously measured OPAL value of $B(\tau^- \rightarrow e^- \bar{\nu}_e \nu_\tau)$ to test various aspects of the Standard Model. In particular, the Standard Model prediction of lepton universality implies that the coupling of the W boson to all three generations of leptons is identical. The leptonic τ decays have already provided some of the most stringent tests of this hypothesis (see, for example, [27]). With the improved precision of $B(\tau^- \rightarrow \mu^- \bar{\nu}_\mu \nu_\tau)$ presented in this dissertation, it is worth testing this prediction again. In addition, the leptonic τ branching ratios can be used to measure the Michel parameter η, which can be used to set a limit on the mass of the charged Higgs particle in the Minimal Supersymmetric Standard Model. These topics are discussed below.

7.1 Lepton universality

Lepton universality requires that the coupling constants g_e, g_μ, and g_τ are identical, thus the ratio g_μ/g_e is expected to be unity, as described in Section 2.4.1. From

Equation 2.9, one finds

$$\frac{g_\mu^2}{g_e^2} = \frac{\mathrm{B}(\tau^- \to \mu^- \bar{\nu}_\mu \nu_\tau)}{\mathrm{B}(\tau^- \to \mathrm{e}^- \bar{\nu}_e \nu_\tau)} \frac{1}{0.9726} \tag{7.1}$$

using $f(m_e^2/m_\tau^2) = 1.0000$ and $f(m_\mu^2/m_\tau^2) = 0.9726$, which are the corrections for the masses of the final state leptons [11]. Equation 7.1 is then used to compute the coupling constant ratio, which, with the value of $\mathrm{B}(\tau^- \to \mu^- \bar{\nu}_\mu \nu_\tau)$ from this work and the OPAL measurement of $\mathrm{B}(\tau^- \to \mathrm{e}^- \bar{\nu}_e \nu_\tau) = 0.1781 \pm 0.0010$ [27], yields

$$\frac{g_\mu}{g_e} = 1.0005 \pm 0.0044,$$

in good agreement with expectation. The OPAL measurements of the branching ratios $\mathrm{B}(\tau^- \to \mathrm{e}^- \bar{\nu}_e \nu_\tau)$ and $\mathrm{B}(\tau^- \to \mu^- \bar{\nu}_\mu \nu_\tau)$ are assumed to be uncorrelated.

In addition, the $\tau^- \to \mu^- \bar{\nu}_\mu \nu_\tau$ branching ratio can be used in conjunction with the muon and τ masses and lifetimes to test lepton universality between the first and third lepton generations, as shown in Equation 2.10, yielding the expression

$$\frac{g_\tau^2}{g_e^2} = \mathrm{B}(\tau^- \to \mu^- \bar{\nu}_\mu \nu_\tau) \frac{(1.678 \pm 0.001) \times 10^{-12}}{\tau_\tau} \ . \tag{7.2}$$

The values $(1 + \delta_{\mathrm{RC}}^\tau) = 0.99597$ and $(1 + \delta_{\mathrm{RC}}^\mu) = 0.99576$, which take into account photon radiative corrections and leading order W propagator corrections, and $f(m_e^2/m_\mu^2) = 0.9998$, have been obtained from reference [11]. These values, along with the OPAL value for the τ lifetime, $\tau_\tau = 289.2 \pm 1.7 \pm 1.2$ fs [29], the BES collaboration value for the τ mass, $m_\tau = 1777.0 \pm 0.3$ MeV [30], and the Particle Data Group [1] values for the muon mass, m_μ, and muon lifetime, τ_μ, have contributed to the numerical factor in Equation 7.2, from which we obtain

$$\frac{g_\tau}{g_e} = 1.0031 \pm 0.0048,$$

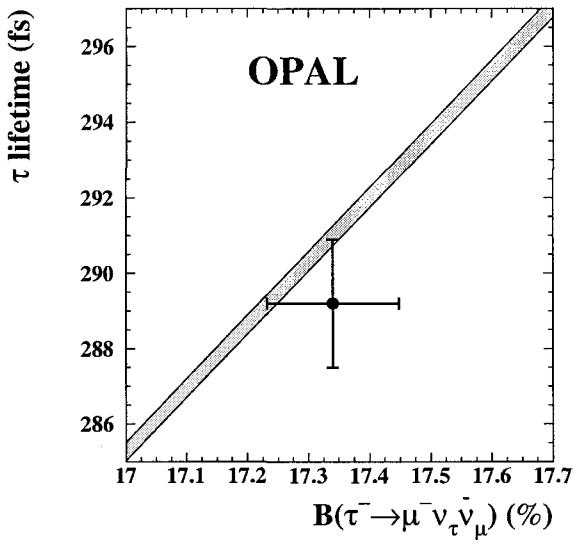

Figure 7.1: The lifetime of the τ vs the $\tau^- \rightarrow \mu^- \bar{\nu}_\mu \nu_\tau$ branching ratio. The band is the Standard Model expectation, and its width is determined by the uncertainty in the mass of the τ [30]. The point with error bars is the OPAL measurement of the τ lifetime [29] and the branching ratio determined in this work.

again in good agreement with the Standard Model assumption of lepton universality. If one assumes lepton universality, then Equation 2.10 can be rearranged to express the τ lifetime as a function of the branching ratio $B(\tau^- \rightarrow \mu^- \bar{\nu}_\mu \nu_\tau)$. The resulting relationship is plotted in Figure 7.1.

The coupling constant ratios presented here are consistent with those obtained using the leptonic τ branching ratios by the other LEP experiments, ALEPH [31], DELPHI [32], and L3 [33], and also with those from the CLEO experiment [34], which uses data from the CESR e^+e^- collider at Cornell State University. The results for each of these experiments is shown in Table 7.1.

Perhaps the most obvious way to test lepton universality in the charged-current weak sector is by using the decay rates of real W bosons; however, to date this method

	g_μ/g_e	g_τ/g_e
ALEPH	1.0002 ± 0.0051	0.9946 ± 0.0064
DELPHI	0.9983 ± 0.0056	0.9987 ± 0.0062
L3	1.0007 ± 0.0051	0.9963 ± 0.0056 *
OPAL	1.0005 ± 0.0044	1.0031 ± 0.0048
CLEO	1.0026 ± 0.0055	1.0043 ± 0.0102 *

Table 7.1: Coupling constant ratios from the four LEP experiments and CLEO. Values with an asterisk were calculated in this analysis using the branching ratio values and τ lifetimes measured by the experiment. All other coupling constant ratios are from the cited references.

has not provided as precise a test as other methods. The two particle colliders with the energies necessary to produce real W bosons are LEP2 at CERN and the Tevatron at Fermilab. The four LEP experiments have presented the combined measurements for the ratios of the W leptonic branching ratios [35]. In this case, the effects of the fermion masses and radiative processes are negligible compared with the precision of the branching ratio measurements, and so no corrections need to be applied to the decay widths; hence, the ratio of the branching ratios simply equals the square of the ratios of the coupling constants, which leads to $g_\mu/g_e = 1.000 \pm 0.011$ and $g_\tau/g_e = 1.026 \pm 0.014$.

The Tevatron collides protons and antiprotons. Because these are composite particles, the total cross section for the interaction will depend upon the specific constituents in the proton and antiproton which interact, and on their energies. Since this varies from one event to the next, the quantity that is measured is the total cross section multiplied by the branching ratio, $\sigma_W B(W \to e\nu_e)$, $\sigma_W B(W \to \mu\nu_\mu)$, and $\sigma_W B(W \to \mu\nu_\tau)$. The ratios of any two of these quantities will produce the square of the ratios of the corresponding coupling constants. Using information from the two Tevatron experiments, D0 [36] and CDF [37], one obtains $g_\mu/g_e = 0.94 \pm 0.05$ and

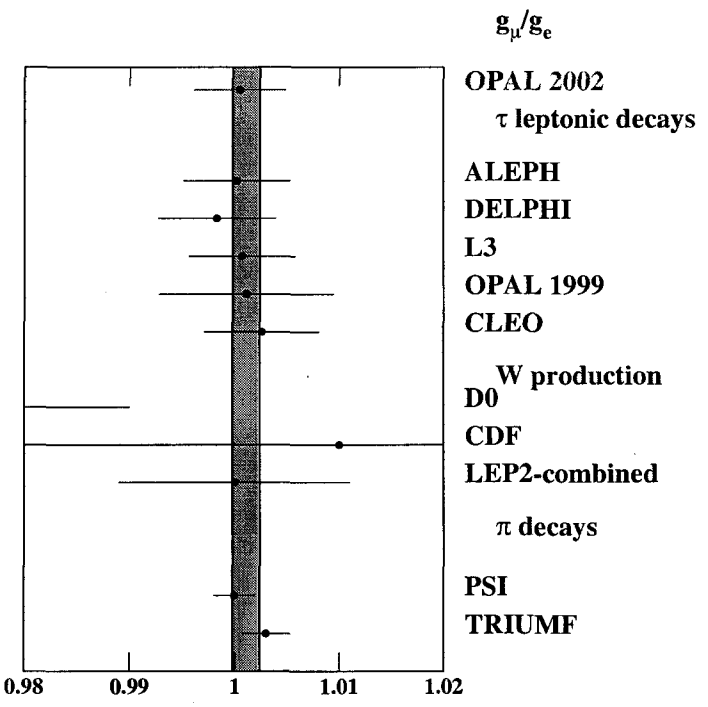

Figure 7.2: g_μ/g_e from various experiments. The band indicates the average of the values plotted.

$g_\tau/g_e = 1.00 \pm 0.03$ for the D0 results, and $g_\mu/g_e = 1.01 \pm 0.04$ and $g_\tau/g_e = 0.97 \pm 0.07$ for the CDF results.

Historically, g_μ/g_e was tested using pion decays, a method which still yields the most precise measurement of this quantity. The two most recent experiments were carried out at TRIUMF [38] and PSI [39], with results of $g_\mu/g_e = 1.0030 \pm 0.0023$ and $g_\mu/g_e = 1.000 \pm 0.002$, respectively. Regardless of the methods used to test lepton universality, the results have been consistent with the Standard Model and with each other. Figure 7.2 shows the results of some of these tests, including the result from this work which is labelled OPAL 2002.

7.2 Michel parameter η and the charged Higgs mass

The leptonic τ branching ratios can be used to probe the Lorentz structure of the matrix element through the Michel parameters [13, 14], η, ρ, ξ, and δ, which parameterize the shape of the τ leptonic decay spectrum, as described in Section 2.4.2. In the Standard Model V-A framework, η takes the value zero. A non-zero value of η would contribute an extra term to the leptonic τ decay widths. This effect potentially would be measurable by taking the ratio of branching ratios, as in Equation 2.15 [15], The $B(\tau^- \to \mu^- \bar{\nu}_\mu \nu_\tau)$ result presented here, together with the OPAL measurement of $B(\tau^- \to e^- \bar{\nu}_e \nu_\tau)$ [27] and Equation 2.15, then results in a value of $\eta = 0.004 \pm 0.037$. This can be compared with a previous OPAL result of $\eta = 0.027 \pm 0.055$ [14] which has been obtained by fitting the τ decay spectrum.

In addition, a non-zero η may imply the presence of scalar couplings, such as those predicted in the Minimal Supersymmetric Standard Model. This leads to the relationship of Equation 2.17. A one-sided 95% confidence limit using the η evaluated in this work gives a value of $\eta > -0.057$, and a model-dependent limit on the charged Higgs mass of $m_{H^\pm} > 1.28 \tan\beta$.

This result is complementary to those obtained using other methods. A similar constraint has been obtained at OPAL using the decay $b \to \tau^- \bar{\nu}_\tau X$, which limits the mass to $m_{H^\pm} > 1.89 \tan\beta$ [40]. At LEP2, charged Higgs particles would have been produced in pairs, via the processes $e^+e^- \to \gamma/Z^0 \to H^+H^-$, with the Higgs particle subsequently decaying to cs or $\tau\nu$. Direct searches using the combined data of the four LEP experiments yielded the limit $m_{H^\pm} > 78.6$ GeV (95% CL) [41]. At the Tevatron, both CDF and D0 use a variety of methods to constrain the charged Higgs mass at both high and low $\tan\beta$, as shown in Figure 7.3. A summary of these

methods is given by the Particle Data Group in reference [1] and further details are available in references [42, 43]. A limit of $m_{\mathrm{H}^{\pm}} > 316$ GeV (95% CL) is given by the Particle Data Group [1] and has been obtained from the rate for the process $b \to s\gamma$ as measured by CLEO [44], BELLE [45], and ALEPH [46]; however, this constraint can be circumvented in supersymmetric models where other particles may contribute destructive interference which cancels out the effect of the charged Higgs. A constraint can be derived given the branching ratio of the decay $\mathrm{Z}^0 \to b\bar{b}$ and other observables, which sets the limit at $\tan\beta > 0.7$ at the 2.5σ level [47, 48]. These are shown in Figure 7.3.

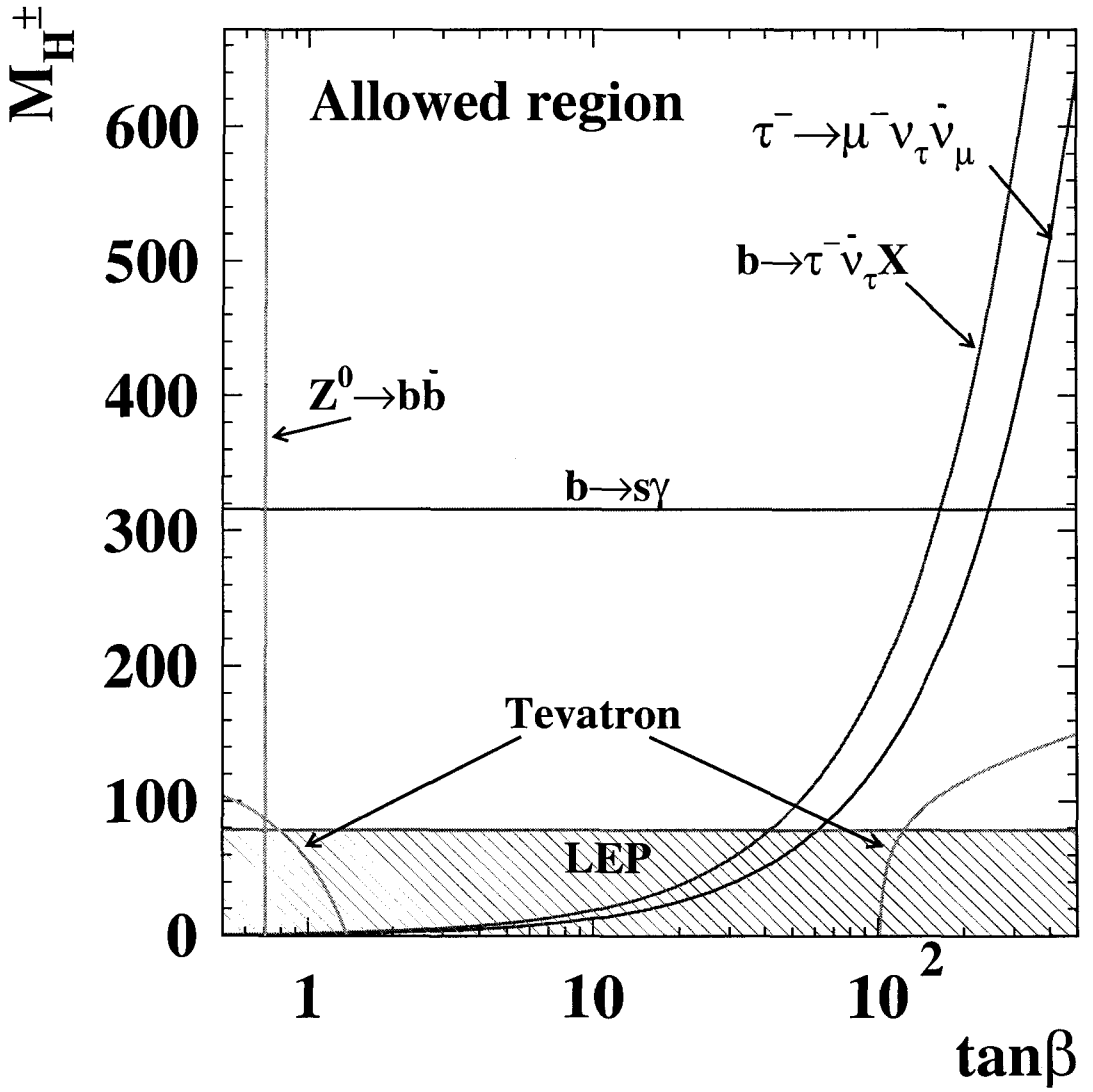

Figure 7.3: Constraints on $m_{\mathrm{H}^\pm}$ as a function of $\tan\beta$ at the 95% CL from this analysis of η using the $\tau^- \to \mu^- \bar{\nu}_\mu \nu_\tau$ decay channel and the other analyses described in the text. The curves for the Tevatron results are approximations based upon information in the references cited in the text.

Chapter 8

Conclusions

OPAL data collected at energies near the Z^0 peak have been used to determine the $\tau^- \to \mu^- \bar{\nu}_\mu \nu_\tau$ branching ratio, which is found to be

$$\mathrm{B}(\tau^- \to \mu^- \bar{\nu}_\mu \nu_\tau) = 0.1734 \pm 0.0009(stat) \pm 0.0006(syst).$$

This is the most precise measurement to date, and is consistent with the previous OPAL measurement [49] and with previous results from other experiments [1], as can be seen in Figure 8.1 which shows other recent results. This work is shown as the OPAL 2002 result.

The branching ratio measured in this analysis, in conjunction with the OPAL $\tau^- \to \mathrm{e}^- \bar{\nu}_e \nu_\tau$ branching ratio measurement, has been used to verify lepton universality at the level of 0.5%. Although lepton universality has been tested to precisions of 0.2% using pion decays, the scalar nature of pions constrains the mediating W boson to be longitudinal, whereas τ decays involve transverse W bosons, making these two universality tests potentially sensitive to different types of new physics.

In addition, these branching ratios have been used to obtain a value for the Michel parameter $\eta = 0.004 \pm 0.037$, which in turn has been used to place a limit on the mass of the charged Higgs boson, $m_{\mathrm{H}^\pm} > 1.28 \tan\beta$, in the Minimal Supersymmetric

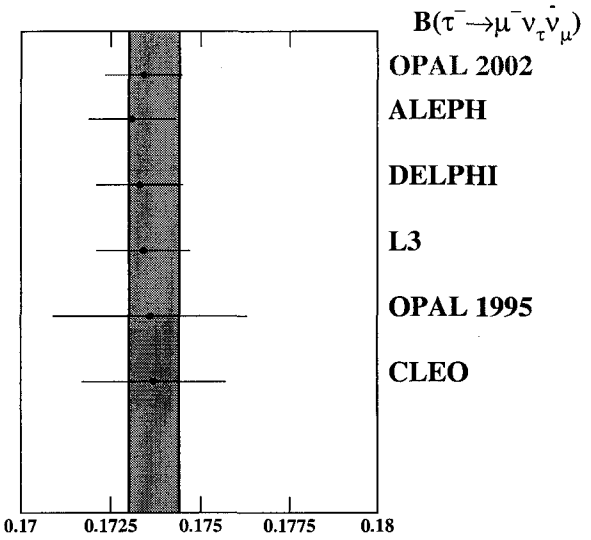

Figure 8.1: $B(\tau^- \to \mu^- \bar{\nu}_\mu \nu_\tau)$ from recent experiments. The shaded band represents the fit from reference [1].

Standard Model. This result is complementary to that from another recent OPAL analysis [40], where a limit of $m_{H^\pm} > 1.89 \tan\beta$ has been obtained from the decay $b \to \tau^- \bar{\nu}_\tau X$.

We use Equation 2.9 to compute the coupling constant ratio, which, with the value of $B(\tau^- \to \mu^- \bar{\nu}_\mu \nu_\tau)$ from this work and the OPAL measurement of $B(\tau^- \to e^- \bar{\nu}_e \nu_\tau) = 0.1781 \pm 0.0010$ [27], yields

$$\frac{g_\mu}{g_e} = 1.0005 \pm 0.0043, \tag{8.1}$$

in good agreement with expectation.

Bibliography

[1] Particle Data Group, K. Hagiwara *et al.*, "Particles and Fields", Phys. Rev. **D66** (2002) 1.

[2] OPAL Collaboration, G. Abbiendi *et al.*, Phys. Lett. **B551** (2003) 35.

[3] S. Glashow, Nucl. Phys. **22** (1961) 579;
S. Weinberg, Phys. Rev. Lett. **19** (1967) 1264;
A. Salam *Elementary Particle Theory*, ed. N. Svartholm., Almquist and Wiksell, Stockholm (1968).

[4] N. Cabibbo, Phys. Rev. Lett. **10** (1963) 531;
M. Kobayashi and T. Maskawa, Prog. Theor. Phys. **49** (1973) 652.

[5] Q. R. Ahmad *et al.*, Phys. Rev. Lett. **89** (2002) 011302.

[6] P. W. Higgs, Phys. Rev. **145** (1966) 1156.

[7] S. Dawson, *SUSY and Such*, Proceedings of a NATO ASI Institute on Techniques and Concepts of High Energy Physics IX, 11-22 July 1996, St. Croix, U.S., Virgin Islands (1996).

[8] G. G. Ross, *Grand Unified Theories*, Frontiers in Physics Lecture Note Series **60**, Benjamin/Cummings Pub. (1984).

[9] S. Dimopoulos, S. Raby, and F. Wilczek, Phys. Rev. **D24** (1981) 1681;
S. Dimopoulos and H. Georgi, Nucl. Phys. **B193** (1981) 150;
L. Ibanez and G. G. Ross, Phys. Lett. **B105** (1981) 439;
N. Sakai, Z. Phys. **C11** (1981) 153;
M. B. Einhorn and D. R. T. Jones, Nucl. Phys. **B196** (1982) 475;
W. J. Marciano and G. Senjanovic, Phys. Rev. **D25** (1982) 3092.

[10] M. L. Perl *et al.*, Phys. Rev. Lett. **35** (1975) 1489;
M. L. Perl *et al.*, Phys. Lett. **B63** (1976) 466.

[11] W.J. Marciano and A. Sirlin, Phys. Rev. Lett. **61** (1988) 1815.

[12] I. Boyko, Nucl. Phys. B (Proc. Suppl.) **98** (2001) 241.

[13] L. Michel, Proc. Phys. Soc. **A63** (1950) 514.

[14] OPAL Collaboration, K. Ackerstaff *et al.*, Eur. Phys. J. **C8** (1999) 3.

[15] A. Stahl, Phys. Lett. **B324** (1994) 121 and references therein.

[16] OPAL Collaboration, K. Ahmet *et al.*, Nucl. Inst. and Meth. **A305** (1991) 275; OPAL Collaboration, P.P. Allport *et al.*, Nucl. Inst. and Meth. **A324** (1993) 34; OPAL Collaboration, P.P. Allport *et al.*, Nucl. Inst. and Meth. **A346** (1994) 476.

[17] S. Anderson, *et al.*, OPAL Collaboration, Nuclear Inst. and Methods **A403**, (1998) 326.

[18] S. Jadach, B.F.L. Ward, and Z. Wąs, Comp. Phys. Comm. **79** (1994) 503.

[19] S. Jadach *et al.*, Comp. Phys. Comm. **76** (1993) 361.

[20] T. Sjöstrand, Comp. Phys. Comm. **82** (1994) 74.

[21] S. Jadach, W. Placzek, and B.F.L. Ward, Phys. Lett. **B390** (1997) 298.

[22] R. Bhattacharya, J. Smith, and G. Grammer, Phys. Rev. **D15** (1977) 3267; J.A.M. Vermaseren, and G. Grammer, Phys. Rev. **D15** (1977) 3280.

[23] J. Allison *et al.*, Nucl. Inst. and Meth. **A317** (1992) 47.

[24] OPAL Collaboration, G. Alexander *et al.*, Phys. Lett. **B266** (1991) 201; OPAL Collaboration, P. Acton *et al.*, Phys. Lett. **B288** (1992) 373.

[25] OPAL Collaboration, G. Alexander *et al.*, Z. Phys. **C52** (1991) 175.

[26] OPAL Collaboration, G. Abbiendi *et al.*, Eur. Phys. J. **C19** (2001) 587.

[27] OPAL Collaboration, G. Abbiendi *et al.*, Phys. Lett. **B447** (1999) 134.

[28] OPAL Collaboration, K. Ackerstaff *et al.*, Eur. Phys. J. **C4** (1998) 193.

[29] OPAL Collaboration, G. Alexander *et al.*, Phys. Lett. **B374** (1996) 341.

[30] BES Collaboration, J.Z. Bai *et al.*, Phys. Rev. **D53** (1996) 20.

[31] ALEPH Collaboration, D. Buskulic *et al.*, Z. Phys. **C70** (1996) 561.

[32] DELPHI Collaboration, P. Abreu *et al.*, Eur. Phys. J. **C10** (1999) 201.

[33] L3 Collaboration, M. Acciarri *et al.*, Phys. Lett. B **507**, (2001) 47.

[34] CLEO Collaboration, A. Anastassov *et al.*, Phys. Rev. **D55** (1997) 2559.

[35] The LEP Collaborations ALEPH, DELPHI, L3, OPAL, the LEP Electroweak Working Group, and the SLD Heavy Flavour and Electroweak Groups, HEP-ex/0112021 **v2** (2002).

[36] D0 Collaboration, S. Abachi *et al.*, Phys. Rev. Lett. **75** (1995) 1456;
S. Protopopescu, $W \to \tau\nu$ *at the Tevatron*, Proceedings of the Fifth International Workshop on Tau Lepton Physics, 14-17 September 1998, Santander, Spain (1998).

[37] CDF Collaboration, F. Abe *et al.*, Phys. Rev. Lett. **69** (1992) 28;
CDF Collaboration, F. Abe *et al.*, Phys. Rev. Lett. **68** (1992) 3398;
CDF Collaboration, F. Abe *et al.*, Phys. Rev. **D44** (1991) 29.

[38] D.I. Britton *et al.*, Phys. Rev. Lett. **68** (1992) 3000.

[39] G. Czapek *et al.*, Phys. Rev. Lett. **70** (1993) 17.

[40] OPAL Collaboration, G. Abbiendi *et al.*, Phys. Lett. **B520** (2001) 1.

[41] ALEPH, DELPHI, L3, and OPAL Collaborations, The LEP Working Group for Higgs Boson Searches, HEP-ex/0107031 **v1** (2001) 1.

[42] CDF Collaboration, F. Abe *et al.*, Phys. Rev. Lett. **79** (1997) 357.

[43] D0 Collaboration, B. Abbott *et al.*, Phys. Rev. Lett. **82** (1999) 4975.

[44] CLEO Collaboration, S. Chen *et al.*, Phys. Rev. Lett. **87** (2001) 251807.

[45] BELLE Collaboration, G. Taylor, XXXVIth Rencontres de Moriond, March 2001.

[46] ALEPH Collaboration, R. Barate *et al.*, Phys. Lett. **B429** (1998) 169.

[47] Aaron K. Grant, Phys. Rev. **D 51** (1995) 207.

[48] M.T. Dova, J. Swain and L. Taylor, Nucl. Phys. B (Proc. Suppl.) **76** (1999) 133.

[49] OPAL Collaboration, R. Akers *et al.*, Z. Phys. **C66** (1995) 543.

Appendix A

The muon chambers

In order to identify muons efficiently, the jet angles θ and ϕ, determined using information from the central tracking chamber, are used to remove events where at least one of the jets extrapolates to a region where there are no muon chambers due to the presence of cables or support structures. The uninstrumented regions are clearly visible in the ϕ versus $|\cos\theta|$ plane shown in Figure A.1, which shows both the barrel and endcap regions of the detector. The values of $\cos\theta$ and ϕ for each of the plotted points is determined using information from the muon chambers only.

The cylindrical geometry of the barrel region is amenable to using a set of cuts in the ϕ versus $\cos\theta$ plane, whereas the structure of the endcap regions is favourable to using a Cartesian set of coordinates. The criteria for accepting an event in the barrel region are given in Table A.1. These criteria map out a boundary which defines the active region of the muon chambers for $\cos\theta < 0.70$, and correspond to the solid line shown in Figure A.1.

A schematic diagram of the endcap muon chamber quadrants and patches in the $x-y$ and $y-z$ planes is shown in Figure A.2 [16]. The fiducial cuts in the endcap region use the jet angle determined from tracking chamber information, extrapolated to the inner faces of the endcap muon chambers, and then converted to Cartesian

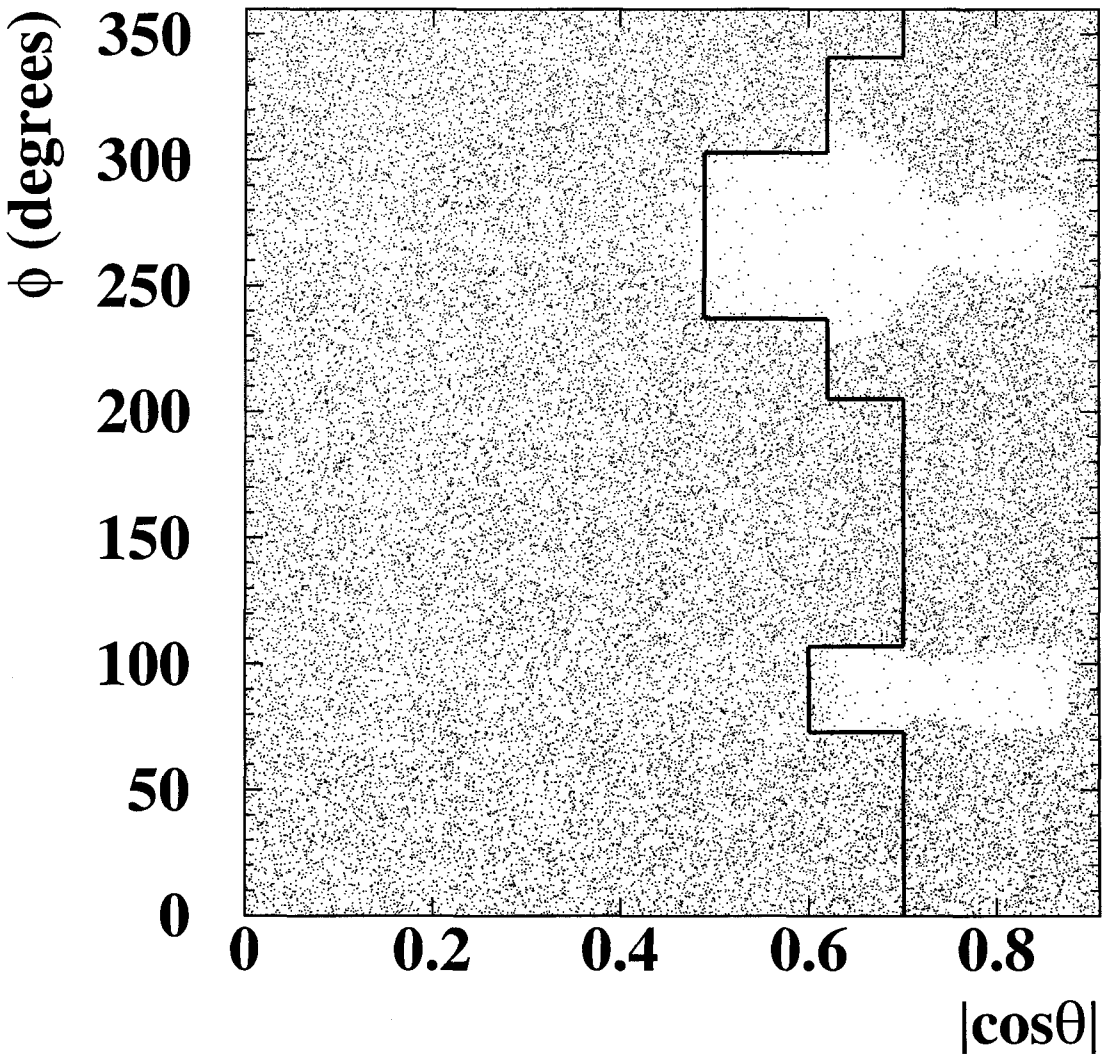

Figure A.1: Muon chamber coverage in the ϕ versus $|\cos\theta|$ plane. The points show regions with signal from the muon chambers. The solid line shows the fiducial cuts in the barrel region.

ϕ (degrees)		$\lvert\cos\theta\rvert$
0 - 73	and	0 - 0.70
73 - 107	and	0 - 0.60
107 - 205	and	0 - 0.70
205 - 237	and	0 - 0.62
237 - 303	and	0 - 0.49
303 - 341	and	0 - 0.62
341 - 360	and	0 - 0.70

Table A.1: Criteria applied to accept only those jets which are in instrumented areas of the barrel muon chambers.

	Inner		Outer	
	lower	upper	lower	upper
Quadrants	553.9 cm	539.0 cm	622.1 cm	606.6 cm
Patches	539.0 cm	554.9 cm	605.6 cm	622.1 cm

Table A.2: The $|z|$ positions of the endcap muon chambers. The positions are the same (within a negative sign) for both endcaps.

coordinates. This information is compared to the coordinates of the muon chambers as shown in the figure. The values are the same for both of the endcaps, except in the case of the y values for the quadrant chambers, where the second set of values is shown in parentheses. The quadrant chambers overlap vertically, but not horizontally. Because of this, the upper and lower chambers are at different z coordinates, as shown in Table A.2 and on Figure A.2 (lower), which gives the z coordinates for the quadrants and patch chambers. Both endcaps have the same $|z|$ values. Each endcap is composed of two sets of chambers, the inner and the outer chambers, where the inner chamber is the one closer to the OPAL interaction point. Figure A.2 shows this in both the $x - y$ plane (upper plot) and the $y - z$ plane (lower plot).

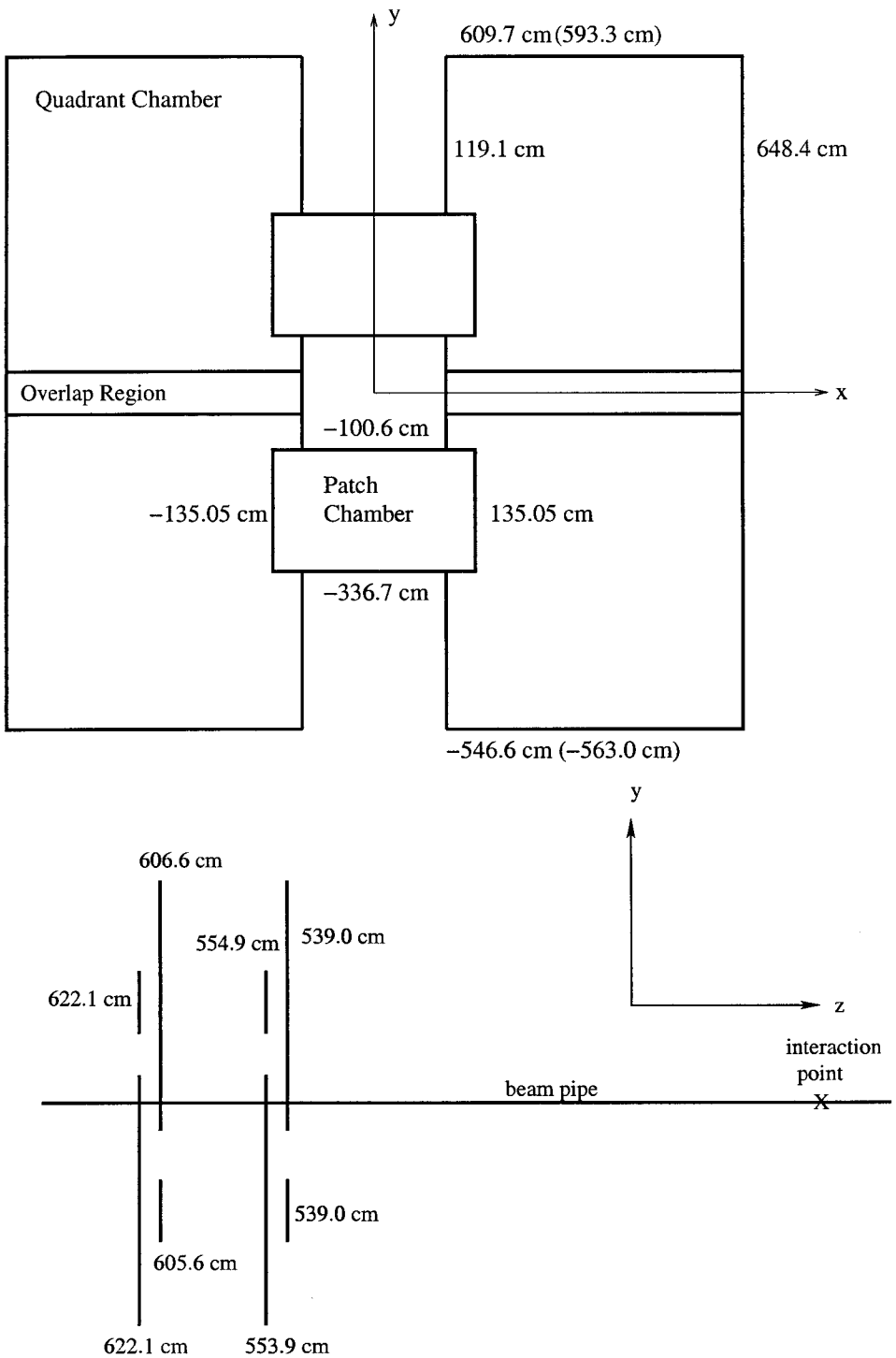

Figure A.2: The endcap regions of the muon chambers in the $x-y$ (upper) and $y-z$ (lower) planes. The quadrant chambers overlap vertically, but not horizontally.

Appendix B

Measuring the backgrounds

The same procedure was used to measure each type of background in the $\tau^+\tau^-$ sample and in the $\tau^- \to \mu^-\bar{\nu}_\mu\nu_\tau$ sample. The relative proportion of the background being measured was first enhanced in the sample by adjusting the selection criteria. Then, a variable was chosen which allowed that particular type of background to be more clearly distinguished from all other events. The Monte Carlo distribution of this variable was fit to the background-enhanced data distribution, where the total number of Monte Carlo events in the i^{th} bin was given by

$$N_i = aN_{\mathrm{sig}_i} + bN_{\mathrm{bk}_i} \ . \tag{B.1}$$

Both a and b were free parameters in the fit, N_{sig_i} is the number of Monte Carlo $\tau^+\tau^-$ or $\tau^- \to \mu^-\bar{\nu}_\mu\nu_\tau$ events in the i^{th} bin, and N_{bk_i} is the number of Monte Carlo events in the i^{th} bin of the type of background being measured. The number of events of other types of background were negligible, and were included in N_{sig_i}. In each case, a was found to be consistent with unity, and therefore was set equal to one.

The fit was performed again with the only free parameter being the normalization of the Monte Carlo prediction of the background being measured, b. The value of b

was determined by a least-squares fit which minimized the χ^2 distribution, given by

$$\chi^2 = \sum_{i=1}^{n} \frac{(N_{d_i} - N_i)^2}{\sigma_{d_i}^2} \tag{B.2}$$

where n is the number of bins in the distribution, N_{d_i} is the number of data events in each bin, and σ_{d_i} is the Poisson error, $\sqrt{N_{d_i}}$, on the number of data events in each bin. The error on the number of Monte Carlo events in each bin was negligible. The error on b was determined by varying the value of χ^2 at its minimum by ± 1. This procedure yielded the scaling factors given in Sections 4.4 and 5.1.

The fractional background in the sample, $f_{background}$, was then determined from the adjusted Monte Carlo simulation, and is given by

$$f_{background} = \frac{N_{bk}}{N} \tag{B.3}$$

where N_{bk} is the total number of Monte Carlo events in the $\tau^+\tau^-$ or $\tau^- \to \mu^-\bar{\nu}_\mu\nu_\tau$ sample of the type of background being measured after the scaling factor is applied, and N is the total number of Monte Carlo events in the $\tau^+\tau^-$ or $\tau^- \to \mu^-\bar{\nu}_\mu\nu_\tau$ sample after all the scaling factors (for each type of background) are applied.

Appendix C

Correlated errors on the scaling factors

Two of the backgrounds, $e^+e^- \rightarrow \mu^+\mu^-$ and $e^+e^- \rightarrow (e^+e^-)\ \mu^+\mu^-$, are present in both the $\tau^+\tau^-$ sample and in the $\tau^- \rightarrow \mu^-\bar{\nu}_\mu\nu_\tau$ sample. For each of these types of background, the scaling factor is the same in both the $\tau^+\tau^-$ sample and in the $\tau^- \rightarrow \mu^-\bar{\nu}_\mu\nu_\tau$ sample, and so the errors associated with these factors are 100% correlated. Because they enter into the branching ratio in a somewhat complicated manner, for this analysis a formula has been derived which takes into account the correlations. The resulting errors on these backgrounds are then added quadratically to the errors from the other backgrounds.

The correlated uncertainty in the branching ratio, σ_B, is

$$\sigma_B = \left(\frac{dB}{ds}\right)\sigma_s \tag{C.1}$$

where σ_s is the uncertainty in the scaling factor as determined by the normalization procedure described in Sections 4.4, 5.1, and Appendix B. For the $e^+e^- \rightarrow \mu^+\mu^-$ correlation, we can write the branching ratio, B, as

$$B = C\left[\frac{1 - f_{other}^{(\tau\rightarrow\mu)} - s f_{\mu\mu}^{(\tau\rightarrow\mu)}}{1 - f_{other}^{\tau\tau} - s f_{\mu\mu}^{\tau\tau}}\right] \tag{C.2}$$

where

$$C = \frac{N_{(\tau\to\mu)}}{N_\tau}\frac{1}{\epsilon_{(\tau\to\mu)}}\frac{1}{F_{\rm b}} \tag{C.3}$$

and $f_{\rm other}^{(\tau\to\mu)}$ ($f_{\rm other}^{\tau\tau}$) is the fractional background in the $\tau^- \to \mu^-\bar{\nu}_\mu\nu_\tau$ ($\tau^+\tau^-$) sample for backgrounds other than $e^+e^- \to \mu^+\mu^-$, s is the $e^+e^- \to \mu^+\mu^-$ scaling factor, and $f_{\mu\mu}^{(\tau\to\mu)}$ ($f_{\mu\mu}^{\tau\tau}$) is the fractional background in the $\tau^- \to \mu^-\bar{\nu}_\mu\nu_\tau$ ($\tau^+\tau^-$) sample of the type $e^+e^- \to \mu^+\mu^-$. Differentiating Equation C.2 gives

$$\frac{\rm dB}{\rm ds} = C\left[\frac{f_{\mu\mu}^{\tau\tau}(1-f_{\rm bk}) - f_{\mu\mu}^{(\tau\to\mu)}(1-f_{\tau{\rm bk}})}{(1-f_{\tau{\rm bk}})^2}\right] \tag{C.4}$$

using the following:

- $s = 1.0$,
- $f_{\rm other}^{(\tau\to\mu)} + sf_{\mu\mu}^{(\tau\to\mu)} = f_{\rm bk}$,
- and $f_{\rm other}^{\tau\tau} + sf_{\mu\mu}^{\tau\tau} = f_{\tau{\rm bk}}$.

Hence, Equation C.1 becomes

$$\sigma_{\rm B} = C\left[\frac{f_{\mu\mu}^{\tau\tau}(1-f_{\rm bk}) - f_{\mu\mu}^{(\tau\to\mu)}(1-f_{\tau{\rm bk}})}{(1-f_{\tau{\rm bk}})^2}\right]\sigma_{\rm s}\ . \tag{C.5}$$

Since the scaling factor for the $e^+e^- \to (e^+e^-)\ \mu^+\mu^-$ background is also equal to unity, the expression for the correlations are exactly analagous to Equation C.5.